Global Teleconnections of Rapid Ionospheric Fluctuations as Observed via GNSS Measurements

Enric Monte-Moreno , Manuel Hernandez-Pajares , and Heng Yang

Abstract—The rapid fluctuations in the electron content of the ionosphere can significantly affect the performance and reliability of communication and GNSS systems. These fluctuations are closely linked to space weather and can result in simultaneous changes in the total electron content of the ionosphere across multiple regions globally. We show the existence of statistically significant synchronous connections between geographical locations when observing fluctuations in electron content. The two findings concerning rapid fluctuations in the electron content of the ionosphere are: 1) evidence of synchronous teleconnections in rapid local electron content variations across a wide range of geographical regions of the globe; and 2) the influence of the solar cycle on the geographic distribution of teleconnections is relatively minor, primarily impacting the frequency of teleconnections per unit of time. We characterize teleconnection patterns for different space weather variables throughout the 2016–2022 study period, encompassing the descending and ascending phases of solar cycles 24 and 25. Previous research has mainly focused on the impact of ionospheric irregularities in limited regions, weather conditions, and short time periods, while our findings indicate the occurrence of this phenomenon globally and during both high and low space weather activity.

Index Terms—Global navigation satellite systems (GNSS), rate of change of total electron content (TEC) index, scintillation, space weather, synchronization, teleconnection, TEC fluctuations.

I. INTRODUCTION

THIS article's significance lies in identifying statistically significant synchronous connections in the fluctuations of electron content between distinct geographical coordinates.

We define these *ionospheric teleconnections* as instances of statistically significant synchrony in total electron content

Enric Monte-Moreno is with the Department of Signal Theory and Communications, TALP, Universitat Politècnica de Catalunya, 08034 Barcelona, Spain (e-mail: enric.monte@upc.edu).

Manuel Hernandez-Pajares is with the Department of Mathematics, IonSAT, Universitat Politècnica de Catalunya, 08034 Barcelona, Spain (e-mail: manuel.hernandez@upc.edu).

Heng Yang is with the School of Electronic Information and Engineering, Yangtze Normal University, Chongqing 408100, China (e-mail: h.yang@yznu.edu.ch).

(TEC) variability among distinct ionospheric regions, exhibiting temporal continuity. Furthermore, we conduct a thorough comparison between the teleconnection phenomenon and various space weather variables, aiming to shed light on its origins. An interesting finding is that while the intensity of space weather impacts the teleconnection patterns, it does not significantly alter their fundamental characteristics.

The approach to long-range interactions in the ionosphere has previously been studied in [1], using network science techniques with a focus on the behavior of TEC in various regions of the globe. Our study, however, takes a different approach by focusing on rate of total electron content (ROTI) rather than TEC values, with a practical emphasis on precise location. One key difference concerns the statistics of ROTI. As identified in a companion article [3] ROTI follows a long-tail distribution, indicating a higher likelihood of outliers compared to a Gaussian distribution. This leads to greater variability in the correlation index which supports our decision to use the cooccurrence method rather than correlation in this article. In addition, since ROTI is tied to rapid TEC fluctuations, we have conducted the study at different time scales.

The rapid local TEC variations across geographically separated regions of the Earth show a coordinated pattern of behavior. This finding is unexpected in the sense that the specific geographical distribution pattern of these synchronized TEC variations does not appear to be dependent on the sun's activity or on *a specific combination* of space weather conditions. This phenomenon is observed across a wide range of distances and latitudes, and it is similar even though the levels of rapid TEC variation (i.e., rate of change of TEC) and the combination of space weather variables are different.

The statistical methods employed in this article to identify significant teleconnections are analogous to those utilized in the study by [2].

A. Aims of This Work

This article aims to provide phenomenological evidence for the presence of teleconnection events in the ionosphere without delving into the physical explanations for such connections and occurrences. In other words, we show that teleconnections are not random events that occur synchronously by coincidence. The physical explanation is multifaceted and reveals consistent patterns throughout the analysis period. This article briefly discusses conjugate points—geomagnetic locations that are magnetically linked and can exhibit similar ionospheric disturbances

simultaneously. Our project consists of two parts: the first article (this one) establishes the statistical fact that statistically significant teleconnections appear in preferential patterns (i.e., pole to pole, pole to equator, and along the equator), and the second article will delve into the details of the underlying phenomena that explain the various types of teleconnections.

This article extends on the work presented in [3], where the authors showed that the distribution of rapid ionosphere electron content fluctuations follows a power law in both amplitude and duration. This was demonstrated using data from over 100 stations worldwide over half a solar cycle.

We use the term *ionospheric teleconnections* to describe the statistical relationship between variations at different points in the ionosphere that are connected over a wide range of distances. We focus specifically on teleconnections involving rapid changes in the TEC. We explore how these changes are connected across a wide range of areas and affect the ionosphere. We also investigate the relationship between these teleconnections and space weather conditions. By studying these teleconnection patterns, we can better understand the features of the ionosphere and how space weather affects them. Furthermore, we examine how changes in TEC at one location are synchronously related to those in another site, highlighting the interconnectivity of the ionosphere.

Finally, we present evidence to support the occurrence of teleconnections in ionospheric activity across various regions of the world, similar to teleconnections observed at the climatic level. Climate teleconnections are global-scale atmospheric and oceanic circulation patterns that affect distant regions' climate conditions. These patterns characterize changes in temperature, precipitation, and other climate variables far away from where the original changes occurred (see for example [2] and [4]). We will employ a measure of rapid TEC variation to identify teleconnections. This measure can be considered an ancillary measure of the scintillation phenomenon. In the methods in Section III-B, we explain how the rapid TEC variation measure relates to the scintillation phenomenon. Using observations from GNSS ground stations, we estimate global maps of rapid TEC variation and establish the synchronicity between geographic coordinates, while assessing statistical significance.

Since space weather is the external cause of rapid TEC variations, it is important to investigate the global patterns of teleconnections by considering different combinations of space weather variable values. Therefore, in all the figures, we present this information through accompanying tables located either inside the maps or in more comprehensive tables below them.

The rapid TEC variation and ionospheric scintillations are characterized by rapid fluctuations in the amplitude, phase, and polarization of radio signals as they propagate through the ionosphere. Scintillation, as well as the rapid variation of TEC, share a common feature: they occur as localized phenomena in small geographic regions and take place in bursts of variable duration.

This article presents evidence for four facts as follows.

1) We present evidence that synchronous teleconnections have been observed in rapid local TEC variations across geographically separated Earth regions, demonstrating a coordinated behavioral pattern (for citations to earlier studies, please refer to the paragraphs below). This phenomenon is observed across a wide range of distances and latitudes. See Section II.

2) The specific geographical distribution pattern of these synchronized TEC variations does not appear to be dependent on the sun's activity or on space weather conditions. This is unexpected, considering that the intensity of TEC variations can differ depending on the phase of the solar cycle. We show that the pattern of teleconnections is similar, although the levels of ROTI, and space weather conditions are different. See Sections IV-A and IV-C.

3) An exception from the previous scenario takes place when some space weather variables reach extreme values, defined as the lower or higher ends of its probability distribution, leading to distinct patterns of teleconnections. See Section IV-C.

4) Statistically significant teleconnections mainly occur at ROTI levels below 0.5 TECUs/min, while teleconnections are nearly absent at higher levels. See Section IV-B.

B. Possible Origins of the Rapid TEC Variation

Rapid TEC variation has various origins that depend on latitude, and a possible classification approach, with a tentative explanation, is as follows.

Case of Low Latitudes: Strong gradients of vertical TEC (VTEC), can be highly localized, especially in the walls of plasma bubbles. Plasma bubbles are large areas of depleted plasma density within the ionosphere that occur at low latitudes. They are magnetic field-aligned plasma depletion structures that develop in the F region over the magnetic equator and grow upward with their extremities passing across the equatorial ionization anomaly and are believed to be caused by a combination of equatorial electrodynamics and atmospheric gravity waves. Equatorial electrodynamics concerns the process of generation of currents and electric fields in the ionosphere through interactive processes in the presence of the Earth's magnetic field. Atmospheric gravity waves are waves in the atmosphere caused by disturbances in the Earth's atmosphere, such as convection, winds, or topography. These waves can propagate upward into the ionosphere and cause the formation of plasma bubbles. The reduced electron density within the "plasma bubbles" leads to rapid changes in the propagation of radio signals passing through the ionosphere, causing ionospheric scintillation. For more details see for instance [5].

Case of High Latitudes: At high latitudes, rapid variations in TEC and scintillation are driven by low-density plasma clusters. These clusters, known as electron density patches, result from various physical processes including ion-neutral collisions and plasma irregularities.

Geomagnetic Conjugacy: The ionosphere responds similarly in both the northern and southern hemispheres to external drivers, such as geomagnetic storms, even though the magnetic field lines are oriented differently in each hemisphere. This means that if a disturbance occurs in one hemisphere, a corresponding disturbance sometimes also occurs in the opposite hemisphere. For a discussion of possible exceptions with physical explanation see for instance [6]. This is because the Earth's

magnetic field is not symmetric, and the ionosphere is highly coupled to the magnetic field.

The explanation that accounts for the locality of the rapid TEC fluctuations falls short of explaining the geographic pattern of the statistically significant teleconnections presented in this research. This requires a physical explanation that considers factors, such as distance and the common occurrence of teleconnections between bursts of moderate ROTI activity. The specifics of this explanation are left to future research.

C. Brief Considerations Related to the Measurements

For this study, we used data obtained from dual-frequency phase measurements of the global navigation satellite system (GNSS) to determine the Rate of Change in the TEC Index (ROTI), which serves as our measure of fast electron content fluctuations. Because the rapid TEC variations are measured between ground stations and satellites, this results in a nonuniform sampling of the ionosphere, which is affected by the position of the satellite relative to the ground station. The ionospheric piercing points (IPP), which are defined as the locations at a specific height in the ionosphere along a straight line between a transmitting antenna and a receiving antenna, are affected by the geographical distribution of ground stations and satellite movements. It is important to note that the location of IPPs changes over time due to the relative trajectories of the satellites and ground stations. The justification of the measurements from GNSS lies in the fact that abrupt changes in the electron content of the ionosphere can cause not only changes in the refractive index of the radio signals associated with GNSS but also diffraction of these signals. The changes in the propagation of the signal can result in varying measurements of TEC along the line of sight. This variability can arise from a combination of physical mechanisms, including atmospheric waves, solar wind-driven disturbances, and geomagnetic storms among others.

The study period covers the years 2016 to 2022, inclusive. The seven-year period includes five years of declining activity in solar cycle 24, followed by two years of increasing activity in solar cycle 25. That is, we cover half a solar cycle that includes the transitions from high to low activity, and then the transition back to high activity.

D. Concepts of Relevance

Next, we define three concepts of relevance for our work as follows.

1) *Ionospheric Piercing Point:* This is the point in the ionosphere where the path between a satellite and a ground station crosses a height where we can assume that the distribution of free electrons is concentrated. This assumption allows us to relate the observed slant and vertical values of the TEC of the ionosphere with limited error.

2) *Ionospheric Teleconnection:* A statistically significant synchrony in the variability of TEC between different ionospheric regions with a temporal continuity of more than 2 min. Regions are defined as grid cells of 0.5×0.5-degrees. See Section III-C for a description and discussion.

3) *Rate of Total Electron Content (ROTI):* A measure of rapid variation of TEC defined as the standard deviation of TEC

over a defined time interval. The ROTI provides information about the dynamic behavior of the ionosphere and is often used as an indicator of ionospheric scintillation. See Section III-B for a description and discussion.

E. Limitations of Previous Studies

One of the limitations of previous studies on explaining TEC variation in terms of ROTI patterns is their limited extent both in terms of specific dates and geographic regions. These studies tend to concentrate on days with geomagnetic storms and provide explanations based on the specific space weather conditions of the event.

For instance, in [7], they identified synchronisms in a region (between $40°$N and $10°$S, and between $90°$E and $130°$E) related to a particular storm during the 20 April 2018. Similarly, the authors in [8] investigated the pole-to-pole stratosphere-to-ionosphere connection in January 2013. In the few cases when the global and time distribution of ROTI is simultaneously analyzed during longer time spans (in [9] during the years 2000, 2009, and 2013), the potential ROTI teleconnections are not considered in the research.

A relevant literature is [10], where the authors provided a physical mechanism that might explain the phenomenon of teleconnections. Although the process of teleconnections has multiple causes, the mechanism outlined in this reference might shed light on the phenomenon.

The apparent delay of the teleconnections detected in this study can reach up to around 5 min in between ionospheric pierce points (IPPs) separated by about 19 000 km. This almost simultaneous apparent ionospheric connection has been observed by different authors in diverse types of specific events, like those associated with the giant ionospheric lamb wave signatures observed in the conjugate northern hemisphere region after Hunga Tonga volcano eruptions [11], the tsunami-driven gravity waves in the ionosphere [12] or the conjugate ionospheric perturbation after solar eclipses [13].

Another article that reports a phenomenon related to teleconnections is [14], which analyzes ionospheric turbulence parameters using data collected during the conjugate point equatorial experiment in Brazil. The article measures scintillation (in our article, due to data availability, we limit ourselves to ROTI measurements) among three locations and detects a propagation phenomenon analogous to a teleconnection.

This article not only aims to establish teleconnections but also to investigate their potential relationship with various space weather variables. To the best of our knowledge, this study is the first to identify the occurrence of teleconnections in the rapid variability of TEC over an extended solar half-cycle period, i.e., during +1600 days, and to examine how different space weather conditions affect these teleconnections.

II. EXAMPLES OF THE GEOGRAPHICAL AND TEMPORAL TELECONNECTIONS

This section presents a set of examples that aim to illustrate the teleconnection phenomenon. The defining property of teleconnections in addition to activity synchronicity across regions, is the persistent bursts of rapid TEC variations. In Figs. 2 and 3
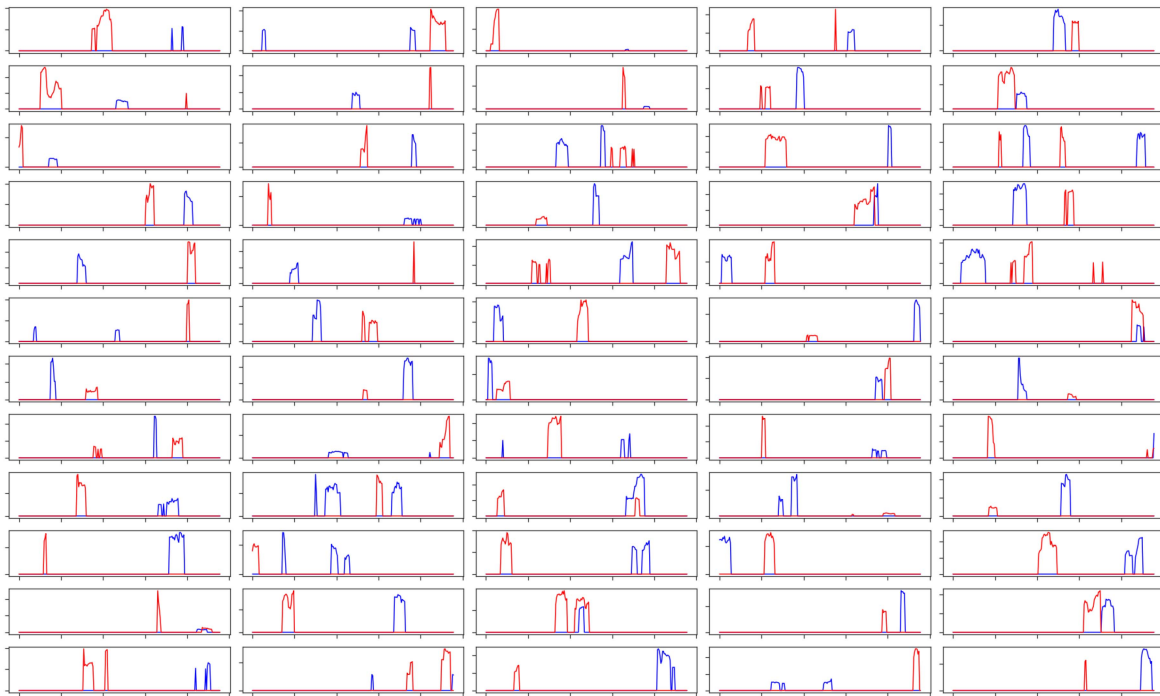
Fig. 1. Examples of ROTI activity for randomly selected pairs of cells (blue: origin, red: destination). DOY 265 of 2016, from 8:30 to 10:30 UTC. The objective of the figure is to show the pattern of overlapping, which is the criterion for deciding the presence of a teleconnection. For the sake of clarity and to illustrate the waveforms, the figures do not include time and amplitude axis values. The x-axis of each subfigure ranges from 8:30–10:30 UTC, and the y-axis of each subfigure spans from 0.05 to 0.5 TECUs/min. For more details, please refer to the main text.

(and in the Appendix Figs. 13, 14, 15), we display the geographic locations and depict the waveform of the ROTI activity at each end of the teleconnection.

The selection criterion for candidate teleconnection coordinates is the activity of each cell during a 24-h interval, with cells defined by 0.5 degrees of latitude and longitude. We will consider cells with a continuous burst lasting more than 2 minutes, and at least one of these bursts must have reached a ROTI of more than 0.5 TECUs per minute. The statistical significance of the teleconnections will be defined in terms of synchronicity in the ROTI activity between regions through a permutation test. For additional details on this topic, please see the Methods Section III-C.

The main feature of ROTI activity is that it appears in continuous bursts starting at specific times. Instances of ROTI activity of duration less than 30 s are rare and appear randomly scattered throughout the measurement interval. As shown in [3], the ROTI activity follows a long-tail distribution in terms of both amplitude and duration. This distribution in terms of duration results in a time series with episodes of bursts of activity followed by periods of inactivity. For further insights into this characteristic of long-tail distributions, see [15], [16], [17], and [18]. This property is significant because it establishes that the p-value obtained from the permutation test serves as an upper bound on the actual value.

Remark: To illustrate the time series of ROTI activity and help to understand the method for identifying teleconnections, we created Fig. 1. This figure presents examples of randomly selected 2-D ROTI time series for different pairs of active cells. The figure provides a snapshot of activity over a 2-h period at various randomly chosen locations. To maintain clarity and avoid cluttering the figure, we intentionally omitted the ROTI levels and time stamps. The x-axis of each subfigure ranges from 8:30 to 10:30 UTC, and the y-axis of each subfigure spans from 0.05 to 0.5 TECUs/min. These details are presented in greater detail in other figures throughout the article, which focus on specific teleconnections. In Fig. 1, the origin and destination are distinguished by color, blue: origin and red: destination. The sudden onset of activity observed in the time series may be attributed to either the intrinsic nature of the phenomenon or the fact that the measurements are obtained from moving satellites. The sudden onset is explained by the statistical properties of the ROTI activity as shown in [3]. It is important to note that the *sampling rate is two samples per minute*, and each time series covers a 2-h range.

Following are the remarks on the selection criteria.

1) A 2-min condition of continuous activity. The general shape of the ROTI time series consists of continuous ROTI activity in the form of bursts, and isolated ROTI values are rare.

2) Cells with at least one burst with ROTI higher than 0.5 TECUs/min in order to include cells with an activity that can affect radio signals crossing the ionosphere.

3) To facilitate the organization of the study, a measurement period of one day is chosen. This is because the bursts of ROTI values typically have a maximum duration of 45 min (with a median of about 8 min). In addition, selecting a one-day measurement period allows for a unit of analysis with sufficient events. (see Table I)

In Figs. 2 and 3, we use different colors to mark the locations of initial (blue) and subsequent activity (red). The examples are measured at 1-h intervals (the caption above each map indicates

Fig. 2.   Examples of five simultaneous teleconnections. *Upper row:* Point to point global Teleconnections (space weather shown in the upper right of the figure). (blue dots: origin, red dots: destination). *Lower rows:* ROTI time series, at each of the teleconections.

Due to software issues, the teleconnections are not depicted as great circles. Due to the issue of clutter, we plotted a common time axis aligned with the bottom row (seconds). The *x*-axis of each ROTI time series ranges across a 1-h interval, (the caption above each map indicates the time of the day). The *y*-axis of each ROTI time series spans 0.05 TECUs/min to 0.7 TECUs/min. The text in between the time series indicates the geographical coordinates of the teleconnection and the relative delay. This text is in a small font to avoid making the figure too large.

TABLE I
DESCRIPTIVE STATISTICS OF THE TELECONNECTIONS

Period	min	25%	50%	75%	max	min	25%	50%	75%	max	min	25%	50%	75%	max
2016−2017	0.5	5.0	7.5	10.5	32.5	55	981	1283	1954	19 725	1	2	4	6	17
2018−2019	0.5	5.5	8.0	11.5	26.0	144	639	1486	2300	18 800	1	2	4	6	20
2020−2021	0.5	5.5	9.0	13.5	32.5	111	863	1344	2090	19 691	1	3	4	7	17
2022	0.5	5.0	7.5	10.5	43.5	55	792	1312	2042	19 424	1	3	5	7	25

Burst Duration [Min] Geodesic Distance [Km] Total #Sim. Teleconn.

the time of the day). In the ROTI time series, we see an overlap between the activity at both ends of the teleconnection with one coordinate having a time lag in relation to the other. Note that at the top of each ROTI time series we provide the teleconnection coordinates and the relative delay. This delay does not necessarily indicate a causal relationship, since the measurements correspond to IPPs, between satellites and ground stations. The absence of a measurement may be due to the fact that there was simply no satellite performing the measurement at that time. We have convincing evidence of a possible systematic temporal relationship between the onsets of activity, however, we leave for a later study of the analysis of the possible causal relationship,

using, for example, the methodology presented in [19] or in [20]. We expand on this point in the methodology Section III-A.

A remarkable feature can be observed in the middle column of Fig. 3, which displays a teleconnection between Brazil and equatorial Africa. The connection from Guinea to Brazil $((-0.1°N, 11°W) \rightarrow (0.02°N, -52°W))$ from 0:00 to 1:00 UTC exhibits a similar waveform, characterized by a sudden onset followed by a gradual descent in the waveform on both sides of the Atlantic. Note that the negative sign is used to indicate a westward direction, while the positive sign is used for an eastward direction. There is a time difference of approximately 3 h between these regions. Plasma bubbles tend to occur post-sunset,
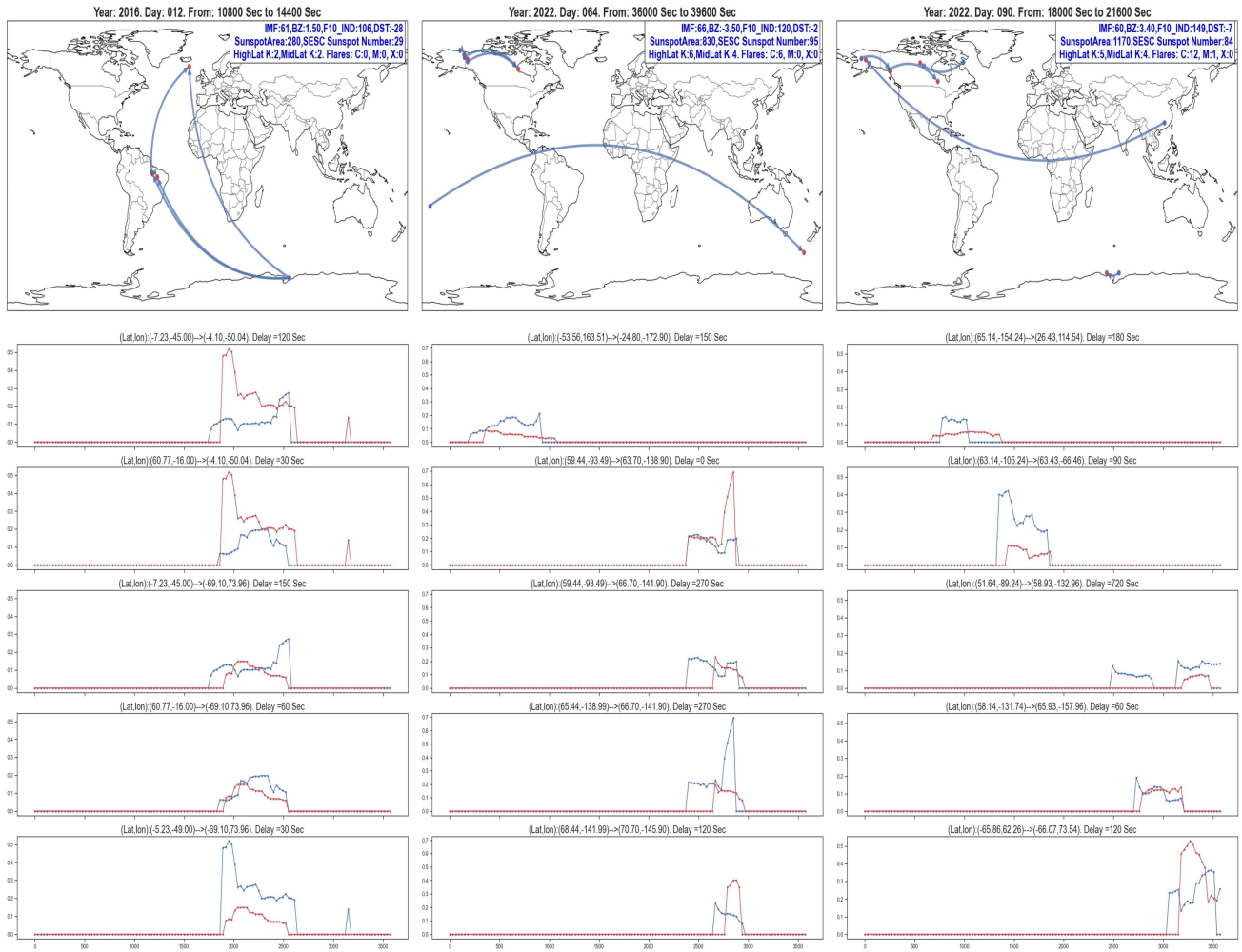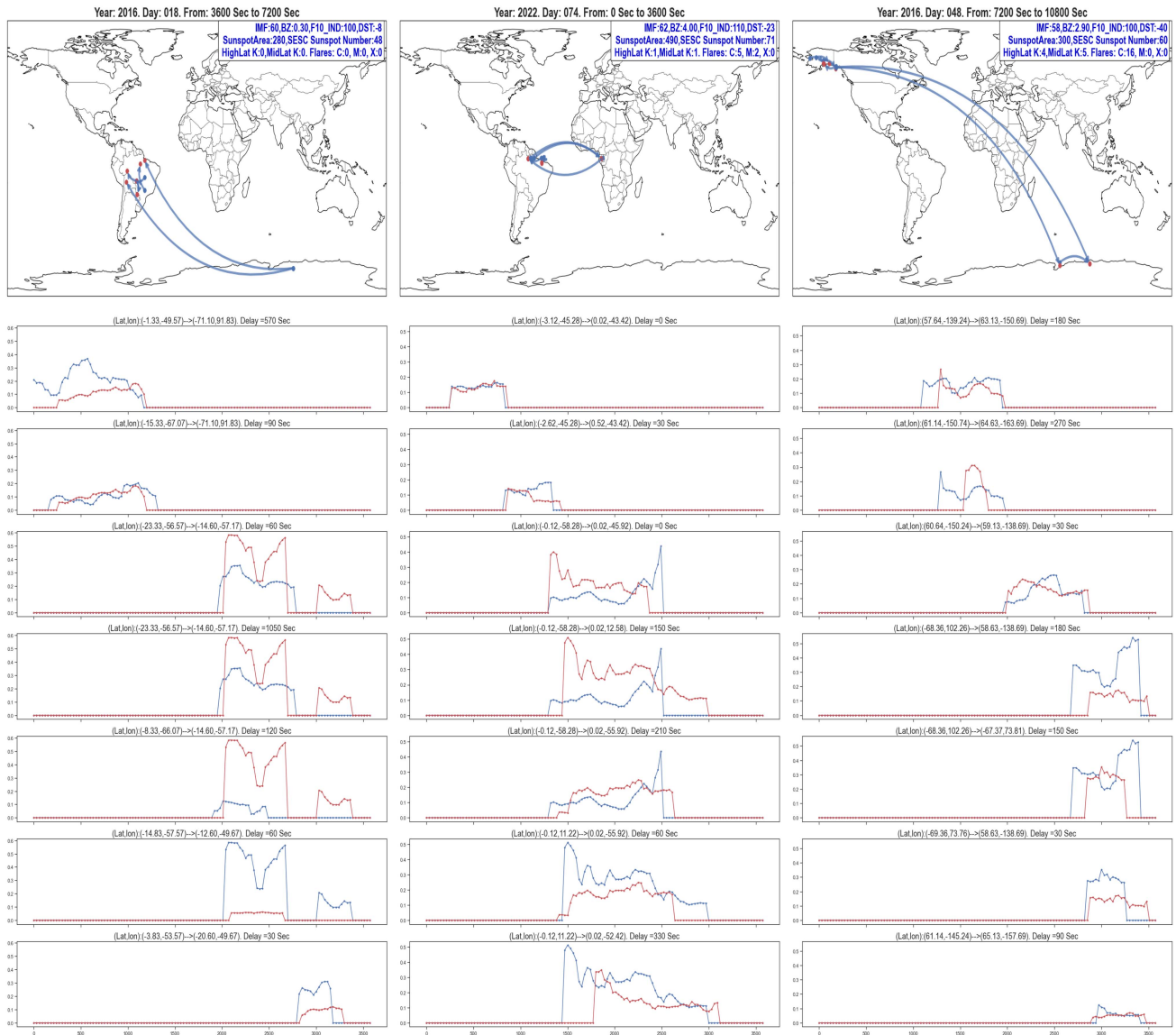
Fig. 3. Examples of seven simultaneous teleconnections. *Upper row:* Point to point global Teleconnections (space weather shown in the upper right of the figure). (blue dots: origin, red dots: destination). *Lower rows:* ROTI time series, at each of the teleconections.
ROTI range: 0.1–0.6 TECUs/min. Due to the issue of clutter, we plotted a common time axis aligned with the bottom row. The *x*-axis of each ROTI time series ranges across a 1-h interval, (the caption above each map indicates the time of the day). The *y*-axis of each ROTI time series spans 0.05 TECUs/min to 0.5 TECUs/min. The text in between the time series indicates the geographical coordinates of the teleconnection and the relative delay. This text is in a small font to avoid making the figure too large.

and irregularities within the plasma bubbles are generated during their growth, subsequently decaying due to diffusion. As a result, the ROTI enhancement at different longitudes appears at different times [21]. On the 15th of March 2022, during the time interval from 0:00 to 1:00 UTC, there is heightened activity observed on the coast of Brazil, while the activity on the coast of Guinea is significantly reduced. In Section IV-B, we will demonstrate that most teleconnections occur within the ROTI range of 0.2–0.5 TECUs/min. Even though during this specific time and date, there were a significant number of events with ROTI values between 0.8 and 1 TECUs/min over Brazil, none of them resulted in a teleconnection. Interestingly, we have observed this phenomenon anecdotally when analyzing various specific scenarios, which suggests that the physical mechanisms

behind ROTI enhancement and teleconnections may be distinct. This observation is also supported by the results presented in Section IV-B.

In Figs. 2 and 3, the spatial distributions of the teleconnections are shown in the upper rows, and in the lower rows are the ROTI time series. The ROTI values associated with the region that activates first are displayed in blue, and those associated with the region that activates later are displayed in red. To improve clarity and highlight the synchronization effect, we show examples with five and seven teleconnections. Additional examples with three, four, and six teleconnections are shown in the Appendix (See Figs. 13 and 14). Table IV in the Appendix provides definitions of the space weather variables mentioned in the figure captions.

Regarding the global distribution of teleconnection distances, the examples conform to the typical distribution, in which short distances are more likely and there is a significant probability of connections between poles (see Table I, and Fig. 7).

Since the probability distribution of the teleconnection features is skewed (see Fig. 7), descriptive statistics, such as median and quartiles are more appropriate for representing the central tendency and variability of the data.

In Figs. 2 and 3, the left column shows an example of a day without solar flares, while the center and right columns depict cases of days with significant solar flare activity. Also, the bursts of activity show continuity.

Note that the depicted teleconnections follow great circles. Due to the map representation centered on the Greenwich meridian, the complementary great circle is sometimes displayed, as seen in the central column of Fig. 2.

The teleconnections show a pattern, where there are pole-to-pole connections and equator-to-pole and teleconnections along similar latitudes. Also, the ROTI waveforms are very similar between very distant coordinates. For example, in Fig. 2 the ROTI waveforms in some teleconnections are similar,

Left column
1) Pole-to-pole Teleconnection: $(60°N, 16°W) \rightarrow (69°S, 74°E)$.
2) Equator-to-pole Teleconnection: $(5°S, 48°W) \rightarrow (69°S, 74°E)$.

Right column
1) Teleconnection inside Canada: $(63°N, 105°W) \rightarrow (63°N, 66°W)$.
2) Teleconnection inside Antarctica: $(65°S, 62°E) \rightarrow (66°S, 73°W)$.
3) Flat ROTI: Guangdong Province, China to Alaska, United States: $(65°N, 154°W) \rightarrow (26°N, 114°E)$.

Fig. 3 shows a very similar waveform appearing in a teleconnection between Brazil and equatorial Africa. In the middle column, connection $(-0.1°N, 11°W) \rightarrow (0.02°N, -52°W)$ that is from Guinea to Brazil, both show a waveform that starts out suddenly and then descends slowly.

These figures serve as a representation of the typical patterns in teleconnection and time series.

The consideration of low ROTI values can affect precise GNSS positioning, which can start on some tenths of TECU/min.

In Figs. 2 and 3, as well as in the Appendix with Figs. 13, 14, 15, which depict cases of teleconnections between both Northern and Southern high latitude stations, one can observe simultaneous fluctuations in electron density in the associated time series (plotted below each map). These synchronous variations between polar regions suggest the presence of geomagnetically conjugate areas connected through magnetic field lines. Changes in one region, such as an auroral substorm, can directly impact its conjugate point through the transfer of particles, momentum, and energy along these field lines. The near-instantaneous responses seen across vast distances indicate the existence of tight coupling along field lines extending between poles. The coordinated high-latitude electron density enhancements visible in opposing hemispheres therefore, provide evidence for magnetically linked conjugate regions.

It remains for a follow-up study to provide a comprehensive analysis of the teleconnections in relation to the geomagnetically conjugate region response for different magnetospheric conditions and space weather drivers. Examining conjugate observations during both quiet and active periods over a range of space weather variables, such as solar wind speed, density, and magnetic field orientation, would provide significant insight into magnetosphere–ionosphere coupling processes. Determining how different solar wind structures, such as coronal mass ejections, corotating interaction regions, and stream interaction regions, affect conjugate locations, in combination with seasonal and time-of-day effects, could reveal details of energy and momentum transfer into the Earth's space environment.

III. METHODS

A. Remarks on Previous Teleconnection Approaches

Climate teleconnections, which model connections between climate conditions in distant regions, serve as inspiration for the concept of Ionospheric teleconnection [2]. Climate teleconnection studies often employ a method developed for analyzing synchrony in biological signals, which determines causal relationships between events [22]. For other applications to climatology, see [23], [24], and [25]. The Event synchronization technique is not suitable for the measurements in this work due to gaps in the time series caused by reliance on satellite trajectories and ground station lines of sight. However, there is evidence of a temporal sequence between teleconnection IPPs, with one group of IPPs in a particular region consistently showing activity initiation before the other, although determining the order is complicated by factors, such as satellite availability and IPP movement.

B. Justification of the Use ROTI

In this section, we justify the use of ROTI as an indirect measure that captures the occurrence of a local scintillation phenomenon.

Ionospheric scintillation causes signal fluctuations in radio waves passing through the ionosphere, leading to errors in navigation and communication systems like GPS and satellites.

Despite their lower sampling rate, TEC measurements obtained from dual-frequency GNSS carrier phases, which define the electron density integral along a line of sight, can still provide informative insights into ionospheric scintillations. This is because the changes in electron density that cause scintillations to occur over a relatively large spatial scale, and TEC measurements provide an average representation of these changes. Thus, TEC measurements are less sensitive to smaller-scale electron density fluctuations. Sufficiently large-scale TEC measurements can still be valuable for studying scintillations, even with a lower sampling rate compared to the scintillations.

The methodology for calculating ROTI, as used in this study, is based on [26], with modifications for improved accuracy at lower elevation angles and implementation of a different mapping function as described in [27] and [28], respectively.

Fig. 4. Maps of Active Stations for the day 365 of the year 2022. Please note that the names of isolated stations are legible, but in regions with a high density of stations, the names may overlap. This map should be viewed more as an indication of the overall distribution of station density.

These references also provide an in-depth discussion of the geometric and implementation considerations involved.

ROTI as a Surrogate for Scintillation: ROTI has been utilized as a replacement for S_4 and σ_ϕ in scintillation detection. In [29], ROTI was compared with S_4 and σ_ϕ for characterizing scintillation occurrences. They examined the correlation between ROTI and scintillation indexes in temporal and spatial domains, using 2-D distribution, Pearson correlation coefficient, and structural similarity as evaluation metrics. Results revealed a strong correlation between ROTI and σ_ϕ in high latitudes, as well as with scintillation during intense and quiet periods. Similar interval calculations for ROTI averages were used in this study as well.

Scintillation levels and ROTI enhancements do not align perfectly due to the distinct scale sizes of the ionospheric irregularities they capture. While ROTI measures a related phenomenon to scintillation, as mentioned in [29], it specifically detects ionospheric irregularities that may cause scintillations. Scintillations predominantly arise from ionospheric irregularities at the scale of hundreds of meters, whereas ROTI targets scale sizes in the range of a few kilometers. Both ROTI and σ_ϕ are based on phase measurements, which account for their similar behavior.

Two other references that show that ROTI provides information that might be used under certain conditions as a surrogate of the scintillations measurements are [30] and [31]. A theoretical model proposed in [32] suggests a link between statistical measures of TEC fluctuations and ionospheric irregularities/scintillations, confirmed by measurements on Ascension Island showing a Pearson correlation index of 0.8 or higher between S_4 and 1-Hz ROTI. Temporal synchronization during rapid increase periods further supports the proposed model, indicating that 1-Hz TEC rate can be a reliable indicator of ionospheric scintillations. This is consistent with previous findings in [33] on the use of ROTI as a scintillation indicator.

In this context, UPC-IonSAT [34] has been computing during recent years ROTI in real time from dual-frequency GNSS measurements of a global network of +100 permanent distributed receivers, within the RT-IGS network represented in Fig. 4.

Ground Stations: Fig. 4 shows the geographic distribution of permanent real-time GNSS ground receivers used in the study. These receivers gather datastreams with a uniform sampling rate of 30 s and a typical latency below 2 s and are processed using the in-house RT-TOMION software developed at UPC-IonSAT to compute VTEC Global Ionospheric Maps and Solar Flare GNSS indexes ([35], [36] and [37]).

Note that the single-layer model of ionosphere is used in the TEC computation, which considers a reasonable balance between accuracy and computational simplicity. The IPP height of model is set to a typical fixed height of 450 km, which approximates a weighted average of the vertical electron density profile ranging from 60–20 000 km approximately (the GNSS transmitter height), effectively representing the altitude where the most part of the free electrons locates, without overemphasizing the peak at lower or higher altitudes, see more details in [27].

The GNSS network is nonuniformly distributed mostly at mid-latitudes resulting in a nonuniform sampling of TEC in the ionosphere reflecting the uneven distribution of detected IPP and stations. The figure displays only active stations as of the last day of the year 2022, which is a subset of the total number of stations used in the study. However, inactive stations represent a small fraction of the total number of stations on any given day, and the number of ground stations available during the study period increased over time.

C. Identification of Statistically Significant Teleconnections

In this subsection, we provide an overview of the process for determining teleconnections, including the statistical methods, variables analyzed, and criteria for significance determination.

Data Organization: The ROTI was computed from TEC measurements at each station, generating global maps with a resolution of 0.5 degrees in latitude and longitude. Maps were created at a rate of *2 per min, i.e., every 30 s*, resulting in 2880 maps per day. Each global map contained 2.592×10^5

cells representing the geographic coordinates. (i.e, 360 degrees of longitude times 180 degrees of latitude times both with a resolution of half a degree). The time-series dimension of each cell, (i.e., geographic coordinate), consists of 4.608×10^6. samples. This requires specifying a partition of the matrix of geographical coordinates matrix times the ROTI samples (i.e., $(2.592 \times 10^5) \times (4.608 \times 10^6)$) in a format that is manageable. The partition of the matrix was done in units of days, to analyze statistically significant teleconnections. This is a natural unit of analysis given the duration and frequency of the ROTI activity bursts (as shown in Table I and Fig. 1), and our process for determining statistical significance. To perform the calculations, we used a data structure consisting of a sequence of daily sparse matrices, each sized 259 200 by 38 400. Teleconnections at temporal extremes may be lost during this processing, especially for bursts of long duration, resulting in potential exclusion of data from the first and last half-hour of a given day. Although this scenario is rare, we believe it does not undermine the descriptive findings presented in this article.

Intuition About the Method: The method relies on defining teleconnections as simultaneous occurrences of ROTI value bursts above a threshold in two or more cells, aiming to detect patterns of activity between cell pairs that occur simultaneously and exceed a certain threshold level of activity. Figs. 2 and 3 show cases in which statistically significant teleconnections were found. while Fig. 1, shows the activity over the same 2-h period for 50 randomly chosen pairs of cells. The above examples suggest that the number of coincidences or synchronizations between cells is a potential statistic for determining the statistical significance of teleconnections through a permutation test.

It is important to note that the number of coincidences is a conservative statistic as it does not consider the temporal continuity of activity, which could result in easier acceptance of the equality hypothesis. This means that the probability of teleconnection by accident is actually lower than this statistical test can give.

The synchronism criterion consisted of counting the common samples between cells in continuous bursts greater than 2 min. The way to achieve this is to create an auxiliary series for each cell. The ROTI values above the minimum threshold are assigned the value one and the counting just consists of a scalar product between the two series. Therefore, the simultaneous activity counting between cells can be expressed as a product of matrices (see following description).

Method for Identifying Teleconnections: The following are the steps involved in processing the data to detect synchronous teleconnections.

1) At each time step ROTI measurements at each IPP were organized into global maps X_{Glob} with a resolution of half a degree creating a 360-by-180 array with a half-degree resolution per timestamp (i.e., $X_{\text{Glob}} \in \mathbb{R}^{(360*2) \times (180*2)}$). The ROTI value of zero was assigned to the coordinates without any measurements.

2) We reshaped the 2-D array X_{Glob} into a vector $x_i \in \mathbb{R}^L$ for each timestamp ($L = 259200$). Each coordinate of the vector x_i corresponds to a given cell (latitude, longitude), and the subscript i denotes a temporal index. The temporal index spans from 0 to N with N being equal to 2880. This

indicates that an observation was recorded every 30 s over a period of one day.

These vectors were concatenated to form the observation matrix, denoted as X, and defined as $X = [x_0, \ldots, x_i, \ldots, x_N]$. The matrix $X \in \mathbb{R}^{L \times N}$ has L rows, which corresponds to the number of cells that the globe is divided into. N columns correspond to the number of observations taken during the day. To fill gaps in one sample within a burst of ROTI, the two neighboring samples were averaged.

To be considered as candidates for testing for teleconnection, cells must meet the following requirements
The cell should have:
a) a minimum of 20 ROTI measurements per day with values exceeding 0.05 TECUs/min;
b) a continuous burst lasting over 2 min during the day;
c) a burst with ROTI values above 0.5 TECUs/min.
The filtering mentioned in the above criterion for candidate cells resulted in a significant reduction in the number of rows in the original matrix, typically by one or two orders of magnitude. The reduced matrix is called X_{red} and the corresponding pairs of tuples (latitude, longitude) are labeled as L_{red}.

3) We created the activity indicator matrix X_{Act} by assigning a value of 1 to any coordinate in X_{red} that exceeded the ROTI threshold of 0.05 TEC units per minute. Next, we calculated the activity cooccurrence matrix X_{Coo} between geographic coordinates using the formula $X_{\text{Coo}} = X_{\text{Act}}^T \times X_{\text{Act}}$. Note that this is a correlation matrix. This means that by performing dot products between all possible combinations of coordinates, the matrix calculates the number of common active elements between the coordinates. The dimension of the resulting matrix is $X_{\text{Coo}} \in \mathbb{R}^{L_{\text{red}} \times L_{\text{red}}}$ indicating the number of times that two different geographic coordinates were active simultaneously during the day. In other words, the matrix X_{Coo} counts the number of observations, where both locations had activity at the same time.

4) To determine the statistical significance of teleconnections, we conducted a permutation test for hypothesis testing (see for instance [38]) on the ROTI time series of each pair of teleconnection candidates. In this test, we used as a test statistic the number of common elements between two cells (as discussed in the following comments). The null hypothesis was defined as cases where the number of common simultaneous coordinates was equal to or greater than the observed case, and 10 000 replicates were performed in the permutation test. We considered a teleconnection to be significant if the p-value was less than 0.0005, that is one in 2000, because as there are multiple comparisons a Bonferroni correction has to be made (see as follows). This means that in the permutation test, a teleconnection was rejected if at least one permutation yielded a number of equal or greater coincidences.

Comments on the Filtering Criterion by ROTI Level: The reason for using this filtering criterion for cells based on the level of ROTI during the day is to detect days when a burst with a high enough ROTI level has occurred. This can be understood

due to the association previously shown of increasing values of ROTI with geomagnetic activity, and the typical duration of geomagnetic activity from several hours to a few days (one example is summarized in [39]). Moreover, such bursts could have an impact on geolocation services, as is the case with single-frequency, or either double-frequency GNSS receivers and telecommunication services. This filtering criterion can help identify possible teleconnections during days of heightened geomagnetic activity, which may be associated with relevant space weather conditions.

In addition to identifying high ROTI bursts that could affect telecommunication and geolocation services, this filtering criterion is also useful for eliminating inaccurate measurements and unexpected ROTI spikes. It maintains the ROTI activity that may be associated with space weather-induced disturbances specific to a certain location and day. Furthermore, it enables the detection of other potential teleconnections during periods when the TEC variability is lower. Teleconnections with low ROTI on active days may occur if they are linked to smaller or more localized ionospheric irregularities that do not generate significant ROTI variations. As an example, see the Figures in Section II.

Comments on the Permutation Test: The definition of the test statistic as the number of common elements between two coordinates is conservative. The test statistic used does not assume any particular sampling distribution, and as such, it does not consider the fact that the ROTI is observed in temporal continuous bursts (see figures in Section II and Fig. 1, for the activity of random pairs of cells). This means that a scattered and discontinuous distribution of activity with the same number of coincidences can be counted as an example of the null hypothesis, and thus, overestimate the number of cases in which the null hypothesis is true. A key point to note is that the ROTI was consistently observed in a burst pattern, and any isolated measurements showing high ROTI could likely be attributed to cycle slips. Furthermore, even for ROTI values that were low, there was a continuous occurrence of these measurements associated with bursts (see for instance bottom plot of [26, Figs. 1, 7, and 8]).

Another issue related to the permutation test is the period of one day. Reducing the period of the permutation test, for instance from one day to one hour raises several issues. First, the sample size of the time series would be smaller, potentially decreasing the test's statistical power. Second, there would be fewer possible permutations, leading to less precise p-values. Third, seasonal or daily patterns in the data could be lost, which could affect the validity of the results. Fourth, the variability in the data may change, which could affect the significance of the results.

The p-value of 0.0005 was chosen for two reasons: 1) to be able to apply the Bonferroni correction of multiple hypothesis tests; and 2) for computational reasons. 1) At any given time there may be up to 50 candidates for teleconnection, with a median value of 17 (with the selection criteria described above), so that with the Bonferroni correction, in the worst case, the corrected p-value is 0.025, in the median case the corrected p-value is 0.0085. 2) The limit of 10 000 repetitions for the permutation test was introduced to make the computation time reasonable. Regarding reliability, it should be noted that in about 130 000 teleconnection candidates, the permutation test with

10 000 repetitions resulted in less than ten rejections. Hence, the probability of accepting a teleconnection by accident is much lower than the 1 in 2000 ratio.

IV. RESULTS

A. Teleconnections Across Various Phases of the Solar Cycle

In this section, we show that teleconnection patterns are similar across different phases of the solar cycle despite variations in space weather conditions. Moreover, we find statistical similarities in the distribution of teleconnection distances during different parts of the cycle.

The study examines the period between the mid-phase of Solar Cycle 24 and the beginning of Cycle 25. Since Cycle 24 reached its peak activity in April 2014, the research concentrated on the declining phase of the cycle, which persisted until the end of 2019 when the Sun entered a state of solar minimum. The investigation also includes the initial phase of Cycle 25, of increasing activity. Fig. 5 (years 2016–2017 and 2018–2019) and Fig. 6 (years 2020–2021 and 2022) include a summary of the space weather conditions during each period. In the Methods Section III-C, we provide details regarding the selection criteria for determining the presence of teleconnections.

The distribution of teleconnections depicted in Figs. 5 and 6 reveals a consistent pattern that persists despite fluctuations in space weather activity. This is shown by the statistics of the space weather variables presented in the tables following the figures. The statistics of the ROTI measurements are discussed in detail in a related publication [3]. The number of significant teleconnections identified during the study period varies significantly with around 1777 detected between 2016 and 2017, 384 between 2018 and 2019, 620 between 2020 and 2021, and 1512 in 2022. Despite this variability, the descriptive statistics—including the minimum, maximum, and percentiles 25%, 50%, and 75%—for the teleconnection distribution remain almost unchanged. This consistency implies that the overall teleconnection pattern remains unaffected by the solar cycle as the statistics remain similar even when the total counts vary by a factor of four. It is important to note that the values for space weather indicators differ significantly in the tables. For instance, the case of Radio Flux at 10.7 cm shows median values ranging from 69–114 SFU, and similar variations can be observed for other variables.

This is shown in a complementary manner in Table I which reveals that the burst duration, the geodetic distance between teleconnected IPPs, and the total number of simultaneous teleconnections all display similar descriptive statistics for each period.

Another significant aspect is the presence of both a high density of local connections and significant long-range connections, as shown in the distance histogram in Fig. 7, and from the statistics of the geodesic distances in Table I.

The observed pattern of teleconnections is related to the accessibility of data from ground stations. The number of stations increased during the period of this study, which explains for instance, why ionospheric teleconnections to China only appeared during the period from 2020 to 2022. Despite the increase in the number of stations during the study period, note that

Years:2016-2017	mean	min	25%	50%	75%	max
BZ	-1	-20.2	-2.4	-1	0.6	8.8
DST	-17.7	-102	-28	-16	-5	30
FlaresX-RayC	0.7	0	0	0	0	16
FlaresX-RayM	0.1	0	0	0	0	7
FlaresX-RayX	0	0	0	0	0	0
EstPlanetaryKInd	3	0	2	3	4	8
HigLatKInd	3	0	1	3	4	9
MidLatKInd	2.5	0	2	2	3	7
RadioFlux10.7cm	81.7	66	74	78	84	140
SESCSunspotNumber	24.9	0	12	22	38	122
SunspotArea	150.1	0	20	80	230	1760

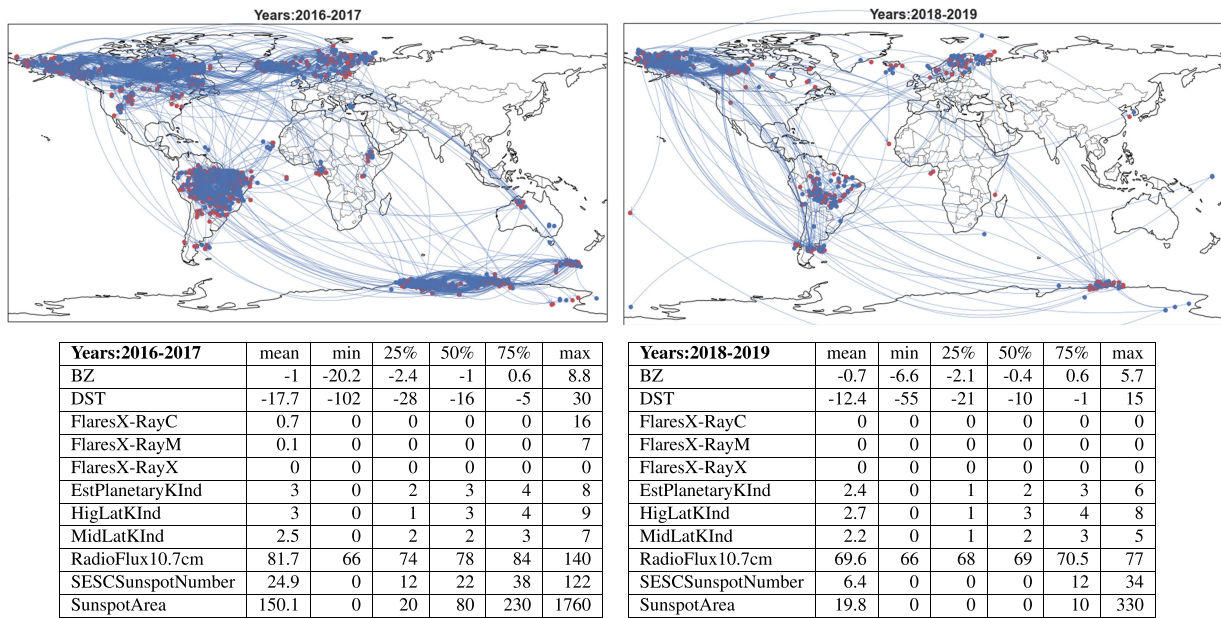| Years:2018-2019	mean	min	25%	50%	75%	max
BZ	-0.7	-6.6	-2.1	-0.4	0.6	5.7
DST	-12.4	-55	-21	-10	-1	15
FlaresX-RayC	0	0	0	0	0	0
FlaresX-RayM	0	0	0	0	0	0
FlaresX-RayX	0	0	0	0	0	0
EstPlanetaryKInd	2.4	0	1	2	3	6
HigLatKInd	2.7	0	1	3	4	8
MidLatKInd	2.2	0	1	2	3	5
RadioFlux10.7cm	69.6	66	68	69	70.5	77
SESCSunspotNumber	6.4	0	0	0	12	34
SunspotArea	19.8	0	0	0	10	330

Fig. 5. Teleconnections and space weather data. Statistically significant teleconnections for the years: (left) 2016 to 2017, and (right) 2018 to 2019. Below, table with Space Weather values for this period. The columns in the table are the descriptive values of each space weather variable, i.e., mean, minimum value, the 25%, 50%, 75% quantiles, and the maximum value.
Due to software issues, the teleconnections are depicted not as great circles but as connecting lines designed to prevent visual clutter.

Years:2020-2021	mean	min	25%	50%	75%	max
BZ	-0.7	-9.8	-2.4	-0.7	0.9	15.9
DST	-8.1	-48	-16	-7	1	28
FlaresX-RayC	2.1	0	0	0	2	15
FlaresX-RayM	0.1	0	0	0	0	2
FlaresX-RayX	0	0	0	0	0	0
EstPlanetaryKInd	2.3	0	1	2	3	6
HigLatKInd	2	0	0	2	3	6
MidLatKInd	1.9	0	1	2	3	6
RadioFlux10.7cm	88.3	68	76	81.5	93.8	140
SESCSunspotNumber	39.5	0	12	26	50.8	147
SunspotArea	271	0	20	135	430	1050

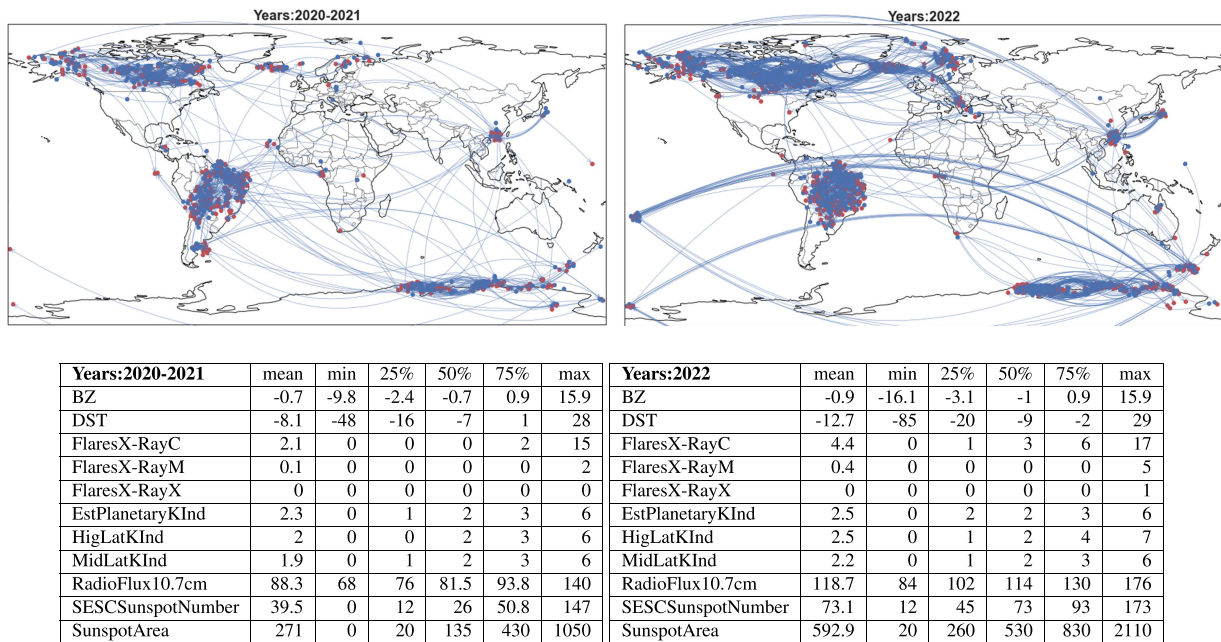| Years:2022	mean	min	25%	50%	75%	max
BZ	-0.9	-16.1	-3.1	-1	0.9	15.9
DST	-12.7	-85	-20	-9	-2	29
FlaresX-RayC	4.4	0	1	3	6	17
FlaresX-RayM	0.4	0	0	0	0	5
FlaresX-RayX	0	0	0	0	0	1
EstPlanetaryKInd	2.5	0	2	2	3	6
HigLatKInd	2.5	0	1	2	4	7
MidLatKInd	2.2	0	1	2	3	6
RadioFlux10.7cm	118.7	84	102	114	130	176
SESCSunspotNumber	73.1	12	45	73	93	173
SunspotArea	592.9	20	260	530	830	2110

Fig. 6. Teleconnections and space weather data. Teleconnections for the years: (left) 2020 to 2021, and (right) 2022. Below, table with Space Weather values for this period. The columns in the table are the descriptive values of each space weather variable, i.e., mean, minimum value, the 25%, 50%, 75% quantiles, and the maximum value.

the pattern of the geographical distribution of teleconnections remains remarkably similar. This observation can be observed through a comparison of Fig. 5 (years 2016–2017) and Fig. 6 (year 2022).

Tables in Figs. 5 and 6 show a similar number and distribution of teleconnections during high activity periods of 2016–2017 and 2022, despite significant differences in space weather indicators. This independence of connection patterns is even more pronounced when comparing high and low activity periods. In low activity periods, space weather indicators differ, but teleconnection patterns remain similar.

Different combinations of space weather values can result in similar teleconnection patterns. However, this fact is often overlooked in literature, which tends to focus on specific solar storms and their details.
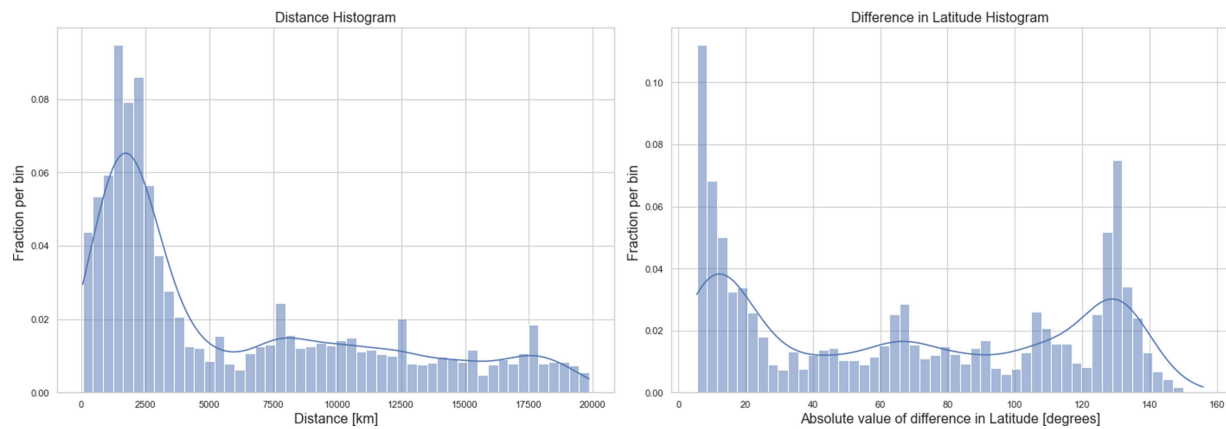
Fig. 7. Histograms of teleconnections. Left: Histogram depicting the geodesic distance (i.e., the shortest distance across the Earth's surface) between teleconnections. Right: Absolute difference in latitude between teleconnections, measured in degrees of latitude.

Fig. 7 displays the normalized histograms representing the behavior of teleconnections in relation to geodesic distance and the absolute difference in latitude. Each bin represents the fraction of teleconnections corresponding to intervals of either distance or latitude difference.

Geodesic Distance Histogram: The histogram on the left of Fig. 7, shows the distribution of distances, which is skewed with a mode between 1500 and 1800 km and a nearly flat distribution from 7000 km onwards, with two small local maxima. This indicates that the most likely teleconnections occur at around 1600 km, but the probability of pole-to-equator or pole-to-pole teleconnections is not negligible. For example, the maximum located at around 10 000 km in the histogram is consistent with a teleconnection between the Porto Alegre GNSS station in Brazil (30.05° S, 51.17° W) and Inuvik Satellite Station Facility (ISSF) in Canada: (68.2° N, 133.4° W), which is 10 600-km apart. The GNSS stations that would measure pole-to-pole teleconnections are separated by a distance compatible with the local maximum of the histogram located at around 17 000 km. For example, the north pole station, Inuvik Satellite Station Facility: (68.2° N, 133.4° W), and the south pole station McMurdo Station GNSS station (77.84° S, 166.66° E) are separated by a distance of 16 500 km.

Absolute Difference of Latitude Histogram: The histogram displays two distinct peaks, representing teleconnections that are more prevalent than others, with one peak near a 5-degree difference and the other at approximately 130 degrees. From Figs. 5 and 6, the peak at the 5 degrees of difference in latitude is explained by the high number of teleconnections between nearby ground stations, which measure the disturbances that affect localized regions. The peaks around 130 degrees can be attributed to the distribution of ground stations and the connections pole to pole. Note that the value of 130 degrees of latitude differences is consistent with the difference in latitude of the ground stations in Antarctica (for example Syowa Station: at 69.0° S; Rothera Research Station: at 67.5° S; McMurdo Station: at 77.8° S) and in the north of Canada/Alaska [for example ISSF: 68.2° N; Fairbanks Alaska Satellite Facility: at 64.8° N; Poker Flat Research Range: at 65.1° N). The latitude differences for these stations are around 140°, which is consistent with the histogram.

The central peak of the histogram, which is around 70 degrees, is consistent with teleconnections, such as those between the northern regions of Canada or the coast of Antarctica and Brazil or China, as depicted in Figs. 5 and 6. Another peak which is represented in the histogram corresponds to a difference of about 110 degrees, which is compatible for example, with the teleconnections between the stations Resolute, Canada (74.6° N) and Hobart, Australia (42.8° S) or Alert, Canada (82.5° N) and Melbourne, Australia (37.8° S)

B. Teleconnections During Extreme ROTI Events

In this section, we investigate the relationship between extreme ROTI events occurring within a single day and the occurrence of teleconnections during the same day. In the previous section, we established a criterion for selecting values greater than 0.5 TECUs/min in the ROTI time series of a specific cell over a one-day period. Now, we will examine the behavior of teleconnections when the selection criterion is more strict. We select days with aN ROTI burst activity of 0.75 TECUs/min or higher within a given time period and analyze teleconnections that occur regardless of the ROTI level.

To illustrate how an increase in ROTI events within a single day impacts the number of teleconnections, Fig. 8 is divided into two parts. The upper rows depict the geographic distribution of teleconnections filtered for varying ROTI levels; specifically, we retained only the teleconnections associated with ROTI values surpassing a defined threshold. The lower rows present tables summarizing the teleconnections discovered for each ROTI level after filtering.

A significant finding in this section is that the presence of teleconnections between ionospheric cells is not always associated with days featuring high ROTI bursts. Increasing the ROTI filtering criterion resulted in fewer selected days, and the proportion of days with teleconnections decreased to a larger degree. Significant teleconnections typically arise during specific time intervals within a day when two bursts occur synchronously. However, the ROTI values of these teleconnections are usually below the maximum value observed during the day.
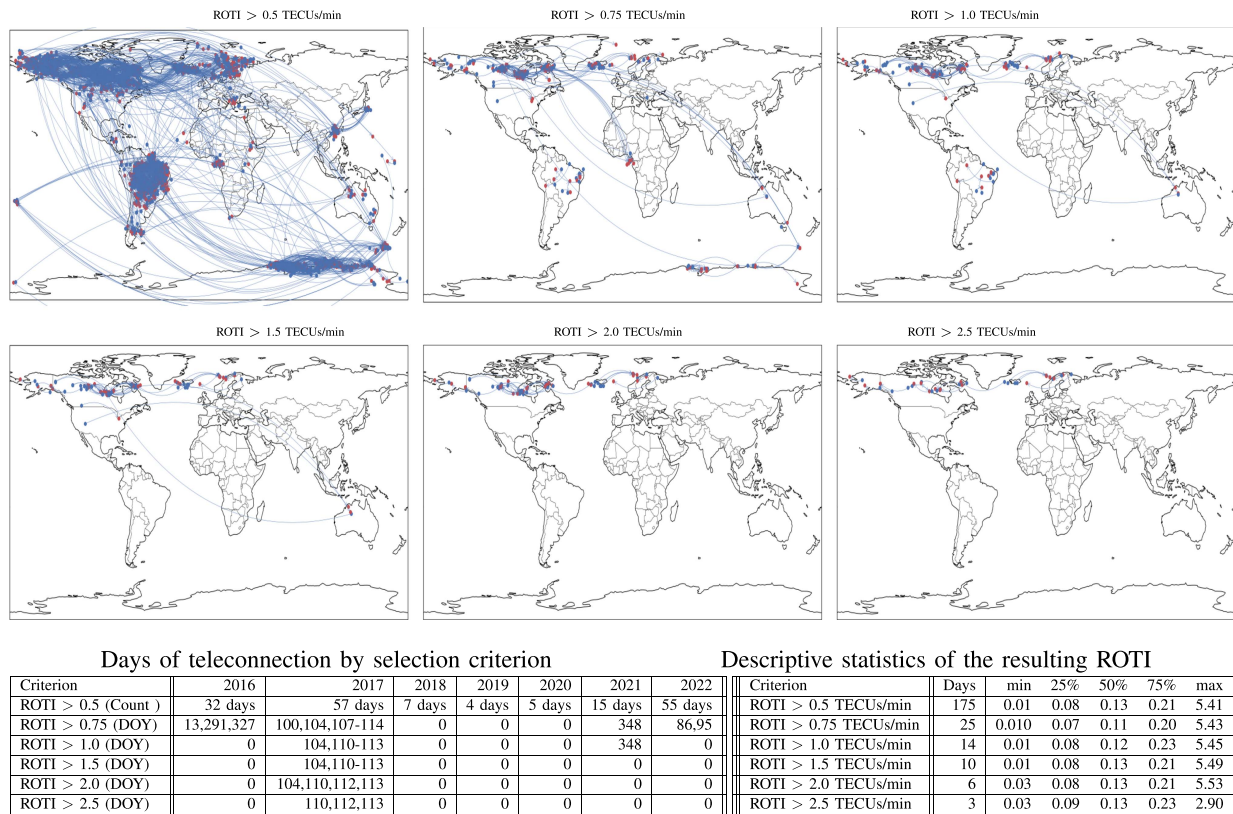
Fig. 8.   Geographical distribution of teleconnections for various ROTI thresholds. The maps illustrate how the count of teleconnections decreases as the ROTI threshold is increased. Table below: Impact of the ROTI threshold on variations in teleconnection count according to Day of Year (DOY), alongside descriptive statistics.

Days of teleconnection by selection criterion

Criterion	2016	2017	2018	2019	2020	2021	2022
ROTI > 0.5 (Count)	32 days	57 days	7 days	4 days	5 days	15 days	55 days
ROTI > 0.75 (DOY)	13,291,327	100,104,107-114	0	0	0	348	86,95
ROTI > 1.0 (DOY)	0	104,110-113	0	0	0	348	0
ROTI > 1.5 (DOY)	0	104,110-113	0	0	0	0	0
ROTI > 2.0 (DOY)	0	104,110,112,113	0	0	0	0	0
ROTI > 2.5 (DOY)	0	110,112,113	0	0	0	0	0

Descriptive statistics of the resulting ROTI

Criterion	Days	min	25%	50%	75%	max
ROTI > 0.5 TECUs/min	175	0.01	0.08	0.13	0.21	5.41
ROTI > 0.75 TECUs/min	25	0.010	0.07	0.11	0.20	5.43
ROTI > 1.0 TECUs/min	14	0.01	0.08	0.12	0.23	5.45
ROTI > 1.5 TECUs/min	10	0.01	0.08	0.13	0.21	5.49
ROTI > 2.0 TECUs/min	6	0.03	0.08	0.13	0.21	5.53
ROTI > 2.5 TECUs/min	3	0.03	0.09	0.13	0.23	2.90

It should be noted that the total number of teleconnection days is influenced by the solar activity of the year under examination. By raising the criterion for ROTI level selection, the number of days with significant teleconnections in 2017 was restricted to only four or five days, despite a tenfold or higher increase in the number of days with ROTI peaks surpassing the selection level. However, the statistical distribution of ROTI values remained consistent for a specific ROTI level requirement when the filtering criterion was increased. This is illustrated by the descriptive statistics table at the bottom of Fig. 8, which shows that the median and interquartile range do not change as the ROTI filtering criterion level increases. The upper part of Fig. 8 shows the geographical distribution of teleconnections during days with high ROTI values, organized by filtering criterion level.

In Fig. 8, the left table displays the dates of teleconnection events throughout the year, except for when ROTI > 0.5 TECUs/min when the number of teleconnections was so high that only the total count is shown. It is worth noting that during dates with ROTI > 0.75 TECUs/min, no significant geomagnetic storms occurred in conjunction with teleconnections. The supplementary Table II includes a list of teleconnection dates and a summary of the top-20 geomagnetic storms. The table also indicates the dates when teleconnections were observed for ROTI levels exceeding 0.75 TECUs/min.

Table III in the extended material shows a clear association of increasing minimum ROTI values with increasing

geomagnetical disturbances, as provided by the sequence of minimum values of Dst index, K-indexes, and either minimum Bz.

Next, we describe space weather conditions on days exhibiting both high ROTI activity and teleconnections, relating these intervals to the rising and declining solar cycle phases. The typical values were compiled from the following sources: [40], [41], [42], [43], [44].

During the dates when the ROTI filtering criterion was higher than 1.0 TECU/min, the Radio Flux at 10.7-cm variable was expected to be between 100 and 150 SFU, but, the maximum observed value was only about 84 SFU. The BZ component of the interplanetary magnetic field was expected to be between −5 and +5 nT, but during these days it reaches a minimum value of −6.8 nT. The DST index, which measures the strength of the ring current in the Earth's magnetosphere, was expected to be between −20 and −50 nT, but the median and maximum values observed during these days (i.e., high ROTI and teleconnection) are greater than expected for the minimum of the solar cycle (range −10 to −20 nT). The planetary K-index, which measures global geomagnetic activity, is expected to be in the range of Kp = 2 to 4, but on these days it is higher, between 6 and 8. The Sunspot Area is expected to be in the range of 10 to 100 millionths of the visible solar hemisphere, but the median and maximum observed values are over 140, similar to values observed during the maximum of the solar cycle. The X-ray flare during these phases is expected to be of C-class and M-class

RadioFlux10.7cm < 68.0 SFU	mean	min	25%	50%	75%	max
BZ	-0.3	-3	-1.3	-0.4	0.5	2.3
DST	-12.1	-49	-20.8	-9.5	-0.5	14
FlaresX-RayC	0	0	0	0	0	0
FlaresX-RayM	0	0	0	0	0	0
FlaresX-RayX	0	0	0	0	0	0
EstPlanetaryKInd	2.3	0	1	2	3	5
HigLatKInd	2.9	0	2	3	4	7
MidLatKInd	2.2	0	1.2	2	3	5
RadioFlux10.7cm	66.8	66	67	67	67	67
SESCSunspotNumber	1.5	0	0	0	0	12
SunspotArea	1.8	0	0	0	0	20

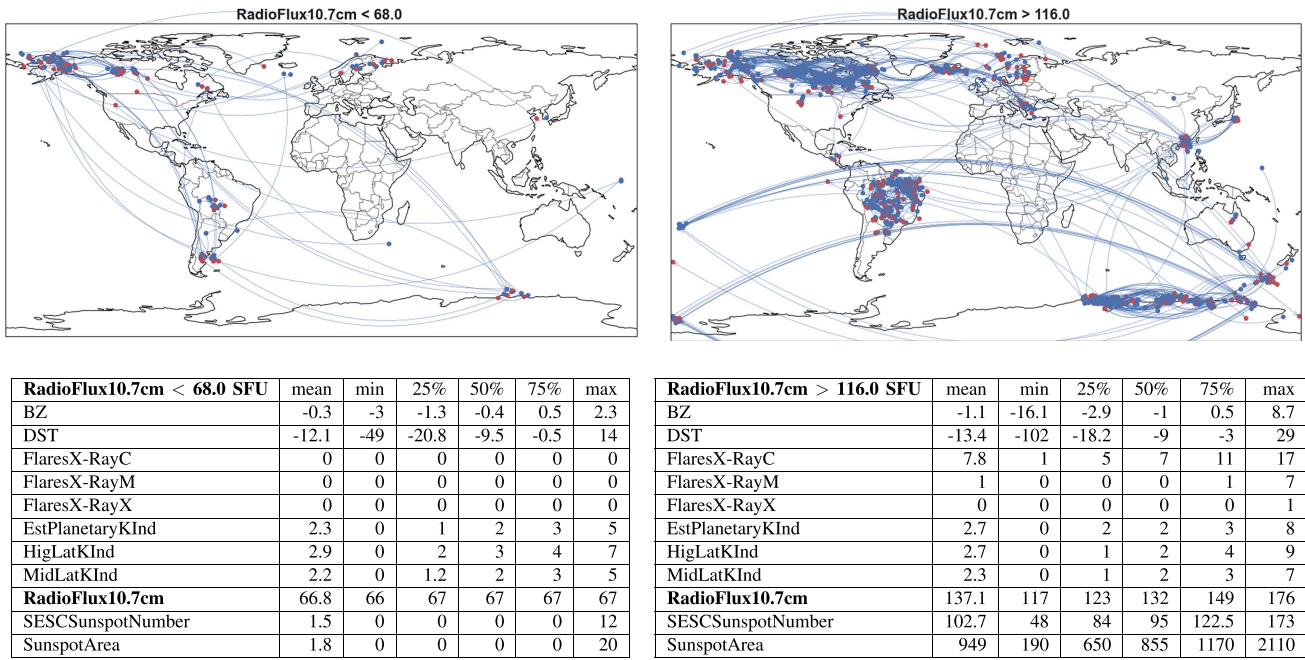| RadioFlux10.7cm > 116.0 SFU	mean	min	25%	50%	75%	max
BZ	-1.1	-16.1	-2.9	-1	0.5	8.7
DST	-13.4	-102	-18.2	-9	-3	29
FlaresX-RayC	7.8	1	5	7	11	17
FlaresX-RayM	1	0	0	0	1	7
FlaresX-RayX	0	0	0	0	0	1
EstPlanetaryKInd	2.7	0	2	2	3	8
HigLatKInd	2.7	0	1	2	4	9
MidLatKInd	2.3	0	1	2	3	7
RadioFlux10.7cm	137.1	117	123	132	149	176
SESCSunspotNumber	102.7	48	84	95	122.5	173
SunspotArea	949	190	650	855	1170	2110

Fig. 9. Radio Flux at 10.7-cm component. Teleconnection distribution patterns for extreme values percentiles 10% and 90%. Space weather values (only for days with teleconnections).
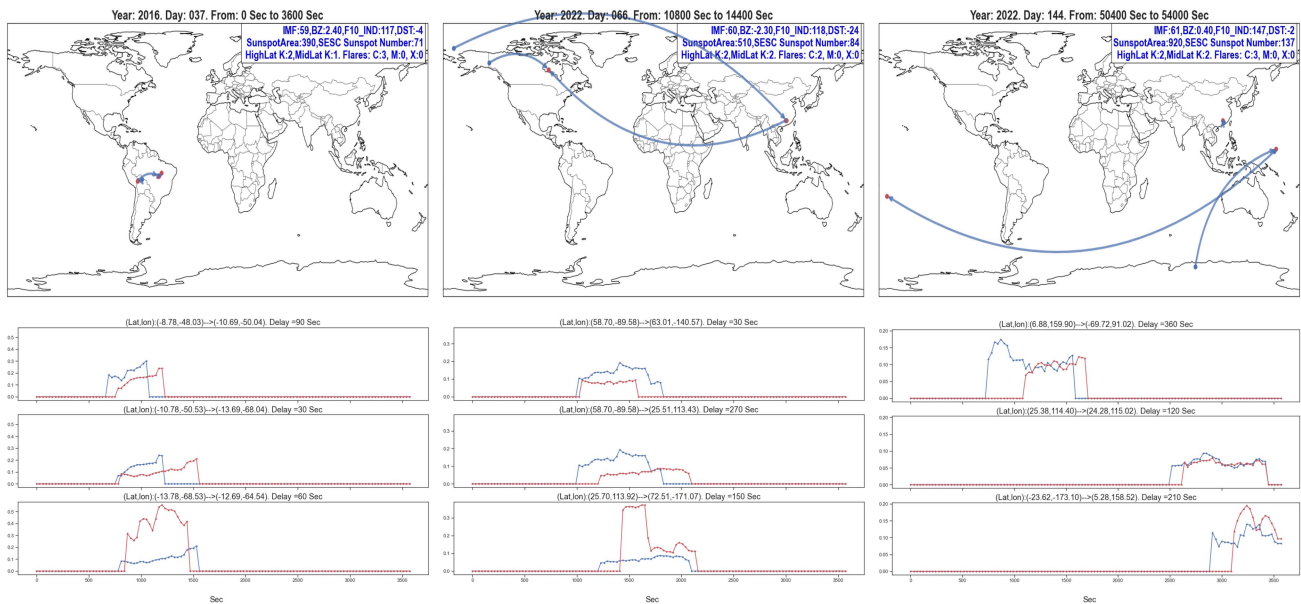

Fig. 10. *Upper row:* Point to point global Teleconnections (space weather shown in the upper right of the figure). (blue dots: origin, red dots: destination). *Lower rows:* ROTI time series, at each of the teleconections, for a threshold of the Radio Flux threshold of > 116.0 SFU (over percentile 90). Note: The space weather status is shown in the upper right of the figure. The *x*-axis of each ROTI time series ranges from 0–3500 s, and the y-axis of each ROTI time series spans from 0.05 TECUs/min to 0.5 TECUs/min.

flares, on the teleconnection days there were only C-class flares similar to the minimum of the solar cycle. The SESC Sunspot Number is expected to be in the range of 50–100 during the declining phase of the solar cycle, the observed value was 43, which is within the normal range of the SESC index.

C. Teleconnections During Extreme Space Weather Events

In this section, we examine the influence of extreme values for space weather on teleconnection location patterns rather than the solar cycle phase. It is important to note that the distribution of connections will differ depending on whether a given space weather variable is at the lower or upper end of its range, and variations in both distance and latitude will also come into play.

Our results show that when space weather parameters do not reach extreme values, the solar cycle does not substantially impact teleconnection distribution. However, we show that extreme magnitudes of individual space weather variables produce unique teleconnection patterns and depart from the solar cycle phase.

BZ < -3.3	mean	min	25%	50%	75%	max
BZ	-5.3	-20.2	-5.6	-4.4	-3.8	-3.4
DST	-22.5	-102	-31.8	-19	-8	29
FlaresX-RayC	2.5	0	0	1	3	17
FlaresX-RayM	0.2	0	0	0	0	5
FlaresX-RayX	0	0	0	0	0	1
EstPlanetaryKInd	3.5	1	3	3	4	8
HigLatKInd	3.6	0	2	4	5	9
MidLatKInd	2.9	1	2	3	3	7
RadioFlux10.7cm	96	68	75	93	112	167
SESCSunspotNumber	43.6	0	14	37	68.8	134
SunspotArea	316.4	0	30	180	447.5	1820

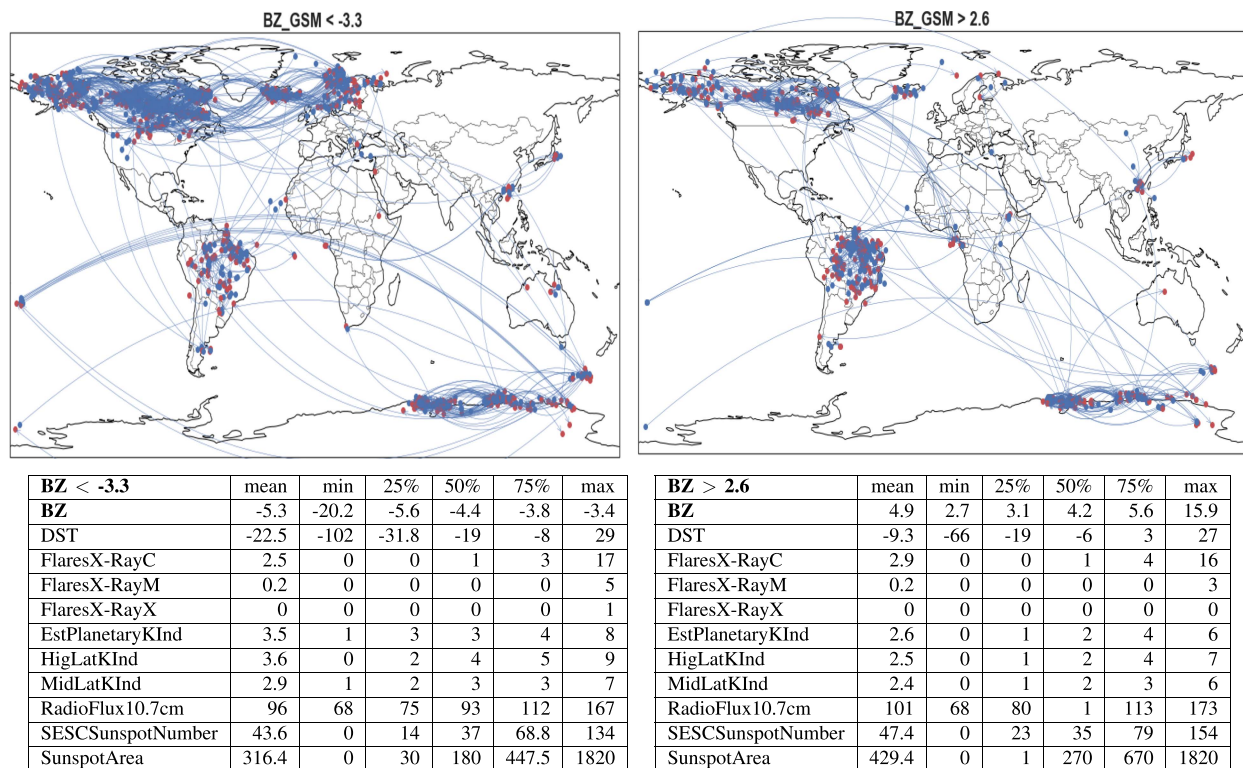| BZ > 2.6	mean	min	25%	50%	75%	max
BZ	4.9	2.7	3.1	4.2	5.6	15.9
DST	-9.3	-66	-19	-6	3	27
FlaresX-RayC	2.9	0	0	1	4	16
FlaresX-RayM	0.2	0	0	0	0	3
FlaresX-RayX	0	0	0	0	0	0
EstPlanetaryKInd	2.6	0	1	2	4	6
HigLatKInd	2.5	0	1	2	4	7
MidLatKInd	2.4	0	1	2	3	6
RadioFlux10.7cm	101	68	80	1	113	173
SESCSunspotNumber	47.4	0	23	35	79	154
SunspotArea	429.4	0	1	270	670	1820

Fig. 11. BZ component. Upper row: Teleconnection distribution patterns for extreme values percentiles 10% and 90%. Space weather values (only for days with teleconnections).

Sigma Bz < 0.4	mean	min	25%	50%	75%	max
BZ	-1.7	-5.8	-3.3	-1.6	0.2	3.1
DST	-8.8	-37	-15.2	-7.5	-1	5
FlaresX-RayC	2.1	0	0	0	3	17
FlaresX-RayM	0.2	0	0	0	0	5
FlaresX-RayX	0	0	0	0	0	1
EstPlanetaryKInd	1.8	0	1	2	3	4
HigLatKInd	1.3	0	0	1	2	5
MidLatKInd	1.5	0	1	2	2	3
RadioFlux10.7cm	90.2	67	73	79	107	150
SESCSunspotNumber	35.5	0	11	24	41.2	124
SunspotArea	261.9	0	10	45	420	1630

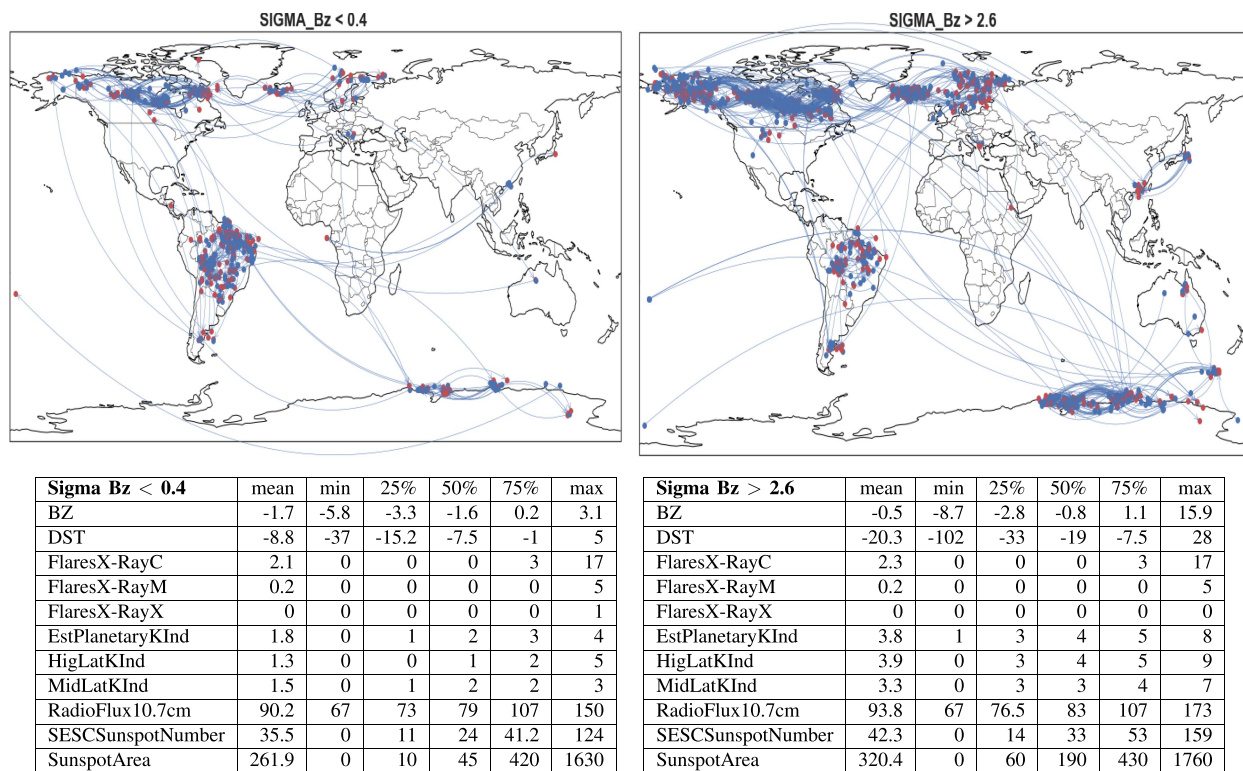| Sigma Bz > 2.6	mean	min	25%	50%	75%	max
BZ	-0.5	-8.7	-2.8	-0.8	1.1	15.9
DST	-20.3	-102	-33	-19	-7.5	28
FlaresX-RayC	2.3	0	0	0	3	17
FlaresX-RayM	0.2	0	0	0	0	5
FlaresX-RayX	0	0	0	0	0	0
EstPlanetaryKInd	3.8	1	3	4	5	8
HigLatKInd	3.9	0	3	4	5	9
MidLatKInd	3.3	0	3	3	4	7
RadioFlux10.7cm	93.8	67	76.5	83	107	173
SESCSunspotNumber	42.3	0	14	33	53	159
SunspotArea	320.4	0	60	190	430	1760

Fig. 12. Sigma Bz component. Upper row: Teleconnection distribution patterns for extreme values percentiles 10% and 90%. Space weather values (only for days with teleconnections).

Note that in this section we show a subset of all possible teleconnections, i.e., those specific to extreme space weather events. For detailed definitions of each space weather variable, please see Table IV in the Appendix.

Definition. Teleconnections during extreme space weather events: refer to teleconnections associated with space weather variable values outside the 10% and 90% percentiles.

Section IV-A showed that the geographic pattern of teleconnections is not significantly affected by the solar cycle when extreme space weather values are not taken into account. In this section, we will focus on individual variables rather than the phase of the cycle when examining how the geographical distribution of connections differs. We will use a filtering criterion based on the extreme values of individual variables. Note that the number of teleconnections will be a subset of the total available. The geographical distribution of teleconnections is greatly influenced by extreme values of variables, such as radio flux at 10.7 cm, sigma-Bz, DST, and KP. This results in different patterns of teleconnections within a hemisphere, changes in pole-to-pole teleconnections, and variations in teleconnection distance. Note that the extreme value of one variable can combine with different levels of the others.

Next, we examine three specific cases of space weather variables.

Remarks on the Extreme Values of Radio Flux at 10.7 cm: During high radio flux periods (i.e., >90th percentile, 116 solar flux units) the ionosphere undergoes increased ionization, resulting in enhanced ionospheric irregularities, such as elevated plasma density. At the equator, the most severe effects of ionospheric irregularities (defined as sudden enhancements and high variability of ROTI) during high radio flux periods are typically observed during equinoxes when the day–night terminator passes over the equator. In higher latitudes, these effects tend to be more widespread and cover larger areas of the globe. In the northern hemisphere, these effects can occur as low as 40 degrees north, while in the southern hemisphere, they can occur as low as 35 degrees south, with severity decreasing at higher latitudes.

During times of high radio flux at 10.7-cm activity levels, (data from [43]) Fig. 9 right, shows that teleconnections are observed for short distances at equatorial and polar areas as well as long-range teleconnections between poles and equator or along the equator. Notably, significant teleconnections are observed between the North Pole and regions between 30 and 40 degrees north latitude, with fewer connections between the South Pole and these medium latitudes in the Northern Hemisphere. In addition, both polar regions exhibit a high density of teleconnections during times of high solar activity.

A representative example is shown in Fig. 10. The ROTI time series for extreme values of the 10.7-cm radio flux resembles those in normal conditions (see Section II). The radio flux ranges from 117–147 SFU with a moderate KP value of 2, and the Sun Spot Area exhibits a wide variation, ranging from 390–920, with two or three class C Flares in all cases. The ROTI shows a range of variation, from 0.05–0.55 TECUs/min. The figures exhibit similar waveforms, time intervals, durations, and amplitudes of ROTI. They show a sudden rise followed by a period of constant ROTI values. For instance, the teleconnections between

two locations approximately 5000-km apart: southeast China (central figure) and Papua New Guinea (right figure). Despite connecting to different poles, these locations exhibit similar patterns.

During periods of low radio flux at 10.7 cm, the ionosphere exhibits reduced ionization resulting in weaker ionospheric irregularities. At the equator, the effects of ionospheric irregularities during low radio flux periods are typically less severe and less frequent compared to high radio flux periods. The effects of the low radio flux condition are seen in the left map of Fig. 9, where the ratio of long-distance teleconnections to connections along the same latitude is higher. This suggests that during periods of low radio flux activity, teleconnections are more likely to occur between the poles and the equator, or between the poles themselves.

Remarks on the Extreme Values of the Bz and Sigma Bz: The orientation of the Bz component with respect to the geomagnetic pole and its variance can lead to two complementary situations, as shown in Figs. 11 and 12. When the Bz component is negative (< -3.3 nT), it is usually associated with high Sigma Bz values (> 2.6 nT), and the teleconnection patterns in both figures are alike. When the Bz component is very negative, it causes a reconnection of both interplanetary and geomagnetic fields, allowing charged particles from the solar wind to easily enter over the geomagnetic poles. This condition is commonly associated with electromagnetic storms and increased scintillation activity. Short-distance teleconnections between latitudes in the polar regions are frequent, and teleconnections also occur between the poles.

A Bz component with a positive orientation greater than the 90th percentile (> 2.6 nT) provides protection by preventing reconnection of the lines near the poles. This leads to lower teleconnection density concentrated around the equator with reduced interpole connectivity. When the variance of Bz is lower than the 10th percentile (< 0.4 nT), the density of teleconnections decreases, and pole-to-pole connections are greatly reduced. Observe the distinct behavior of the teleconnections based on extreme values of sigma Bz. In the case of sigma Bz values in the lower 10th percentile, the teleconnections tend to concentrate over Brazil, likely influenced by the availability of stations during the study period. On the other hand, for sigma Bz values exceeding the 90th percentile, the teleconnections exhibit a significantly higher density in the polar regions.

Considerations Regarding the Shape of the ROTI Time Series: At times of extreme values of space weather variables, the teleconnection ROTI time series exhibits minimal changes in terms of amplitude range, burst duration, and relative delay. To illustrate this we consider two cases in addition to Fig. 10.

For extreme values of Bz (see Fig. 16, $Bz < -3.3$ nT and Fig. 17, $Bz > 2.6$ nT in the Appendix), the ROTI time series tends to exhibit similar shapes in amplitude and burst duration, as shown in Section II. In these cases, the Kp values are around 3 or 4. Unlike the case of extreme Radio Flux at 10.7 cm, these examples have lower Radio Flux values of around 70 SFU and significant variation in Sun Spot number. While the sign of Bz primarily determines the difference in latitude of teleconnections, these examples display teleconnections between poles and along similar latitudes.

Fig. 18 (Appendix) shows the time series for an extreme scenario where there are more than ten flares of class C or higher in a single day. The amplitude and duration ranges of ROTI bursts are similar to previous cases. However, in this example, the values of other spatial climate variables are notably high. Moreover, the teleconnection pattern still reveals connections between poles and along similar latitudes.

V. CONCLUSION

The key finding presented in this article is that rapid fluctuations in electron content across geographically separated regions of the ionosphere are synchronized. Statistical analysis shows significant teleconnections between TEC variations at different locations, even over long distances. Surprisingly, the spatial patterns of these connections do not seem to depend on solar activity or space weather conditions. This suggests that ionospheric teleconnections are primarily associated with geomagnetic activity. Although space weather intensity may impact the number and strength of teleconnections, the proportion of connections across different distance ranges remains consistent. This indicates that the distribution of teleconnections is largely independent of specific space weather events. The results provide evidence for synchronous electron content fluctuations at global scales that could influence communication and navigation systems worldwide.

The nonuniform distribution of GNSS stations influences the detection of teleconnections, particularly in regions with sparse coverage. This results in observing only a subset of possible teleconnections. For instance, in Fig. 5 (years 2016–2017), there are no teleconnections to China, whereas in Fig. 6 (year 2022), a significant number of teleconnections appear. These differences cannot be attributed to space weather but are instead due to the availability of new stations. Moreover, we are unable to determine the pattern of teleconnections related to parts of Africa, Siberia, or the oceans.

An important contribution of the findings in this article is that the approach might be used for doing forecasts of these variations to improve the accuracy and reliability of GNSS-based navigation. While previous forecasting systems relied on smoothed forecasts based on diffusion principles [45], the use of the information provided by the teleconnections may provide a more effective way to generate localized forecasts in restricted regions.

The line of work will be related to studying the relationship of connections not as a point-to-point phenomenon but as a diffusion phenomenon of connections. In addition, we aim to apply the findings in [3], which demonstrate a power law behavior of rapid ionospheric fluctuations. One defining characteristic of time series exhibiting power law behavior is the manifestation of bursts of continuous activity. By understanding the shape parameter of the power law distribution, one can establish confidence intervals for joint activity between different points in the ionosphere, as well as determine the trajectory of connections between points.

Another relevant finding is the varying dependency of teleconnections on different space weather conditions. This variability might enable the introduction of priors into the statistics of machine learning tools used to predict the future evolution of ionospheric perturbations.

This article also presents a statistical framework demonstrating the existence of ionospheric teleconnections but leaves the underlying physical mechanisms for future study. The findings give insight into how local disturbances in the ionosphere may spread globally through rapid changes in electron content. By revealing connections across vast distances, the work highlights the importance of understanding teleconnections for mitigating space weather impacts on technology.

The findings presented in this article are significant because the ionosphere is a region of the Earth's upper atmosphere containing charged particles playing a crucial role in the reflection and refraction of radio waves. By detecting teleconnections in real time, one can use this information to identify simultaneous communication disruptions, especially in high-frequency and very high-frequency bands. This is particularly problematic for long-distance communication, such as aviation and maritime communication. In addition, it may help in pinpointing locations experiencing simultaneous increases in GNSS errors. Rapid ionospheric fluctuations can induce changes in signal phase and amplitude leading to errors in position determination. This is a major concern for applications like navigation, where accuracy is crucial. Furthermore, these fluctuations can impact the quality of observations and data collected by radio telescopes positioned at various locations.

One of the inherent limitations of the method employed in this study is that it is designed to detect synchrony only between consecutive events. As a result, it is well suited for identifying synchronicity over short timescales typically ranging from seconds to about an hour. This makes the ROTI index an appropriate choice for capturing rapid fluctuations in ionospheric activity. However, more complex interactions, particularly those involving specific rhythms or periodic frequencies over longer time intervals, are more challenging to detect using the current approach. Future work could explore the development of methods capable of capturing these more intricate interactions. Such methods may require additional parameters or different time-series analysis tools, which can account for nonconsecutive events and detect periodicities over broader temporal scales. By expanding the scope of the analysis, we could gain a deeper understanding of the underlying dynamics in the ionosphere and the associated teleconnections.

This work reveals patterns of teleconnections that are influenced by both the solar cycle (as shown in the space weather statistics provided for each figure) and the distribution of stations. Due to variations in space weather statistics, the global distribution of teleconnections was slightly different at both peaks of solar activity during the study period, which might partly explain this effect. Another potential explanation is the increase in the number of stations in 2022. For instance, there are stations in mainland China that were not available during the 2016/17 period. Therefore, the regions with weaker connectivity could either result from a lack of available stations or reflect an underlying physical phenomenon, such as a lower density of teleconnections over mid-latitudes. However, this does not invalidate the finding that there are statistically significant patterns of teleconnections.

Fig. 13.   Examples of three simultaneous teleconnections. Upper row: Teleconnections (space weather indexes shown in the upper right of the figure). Lower rows: ROTI time series. ROTI range: 0.1–1.0 TECUs/min.
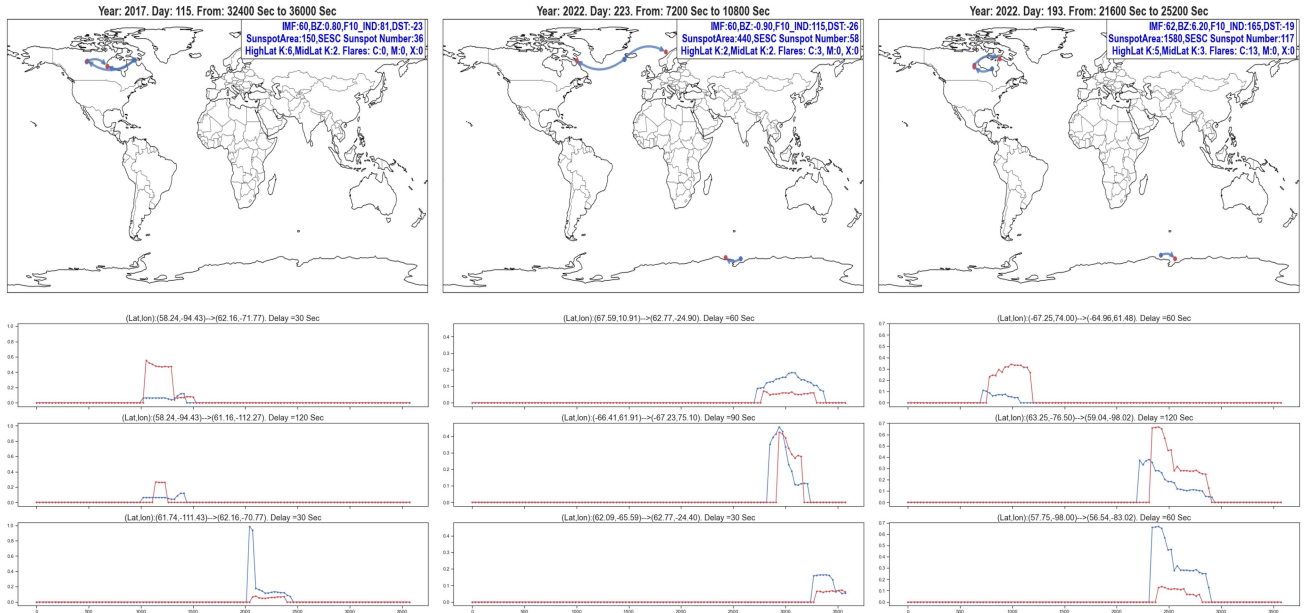

Fig. 14.   Examples of four simultaneous teleconnections. Upper row: Teleconnections (space weather indexes shown in the upper right of the figure). Lower rows: ROTI time series. ROTI range: 0.1–0.65 TECUs/min.

Fig. 15. Examples of six simultaneous teleconnections. Upper row: Teleconnections (space weather indexes shown in the upper right of the figure). Lower rows: ROTI time series. ROTI range: 0.1–0.6 TECUs/min.
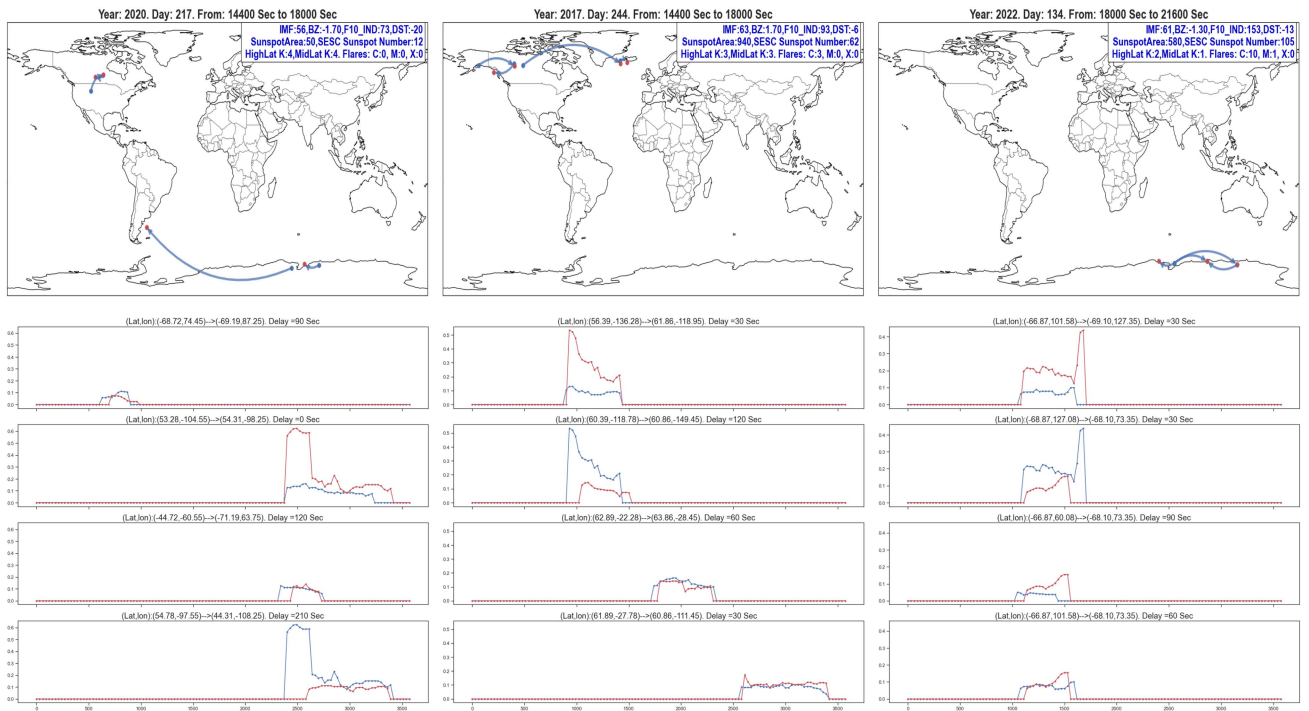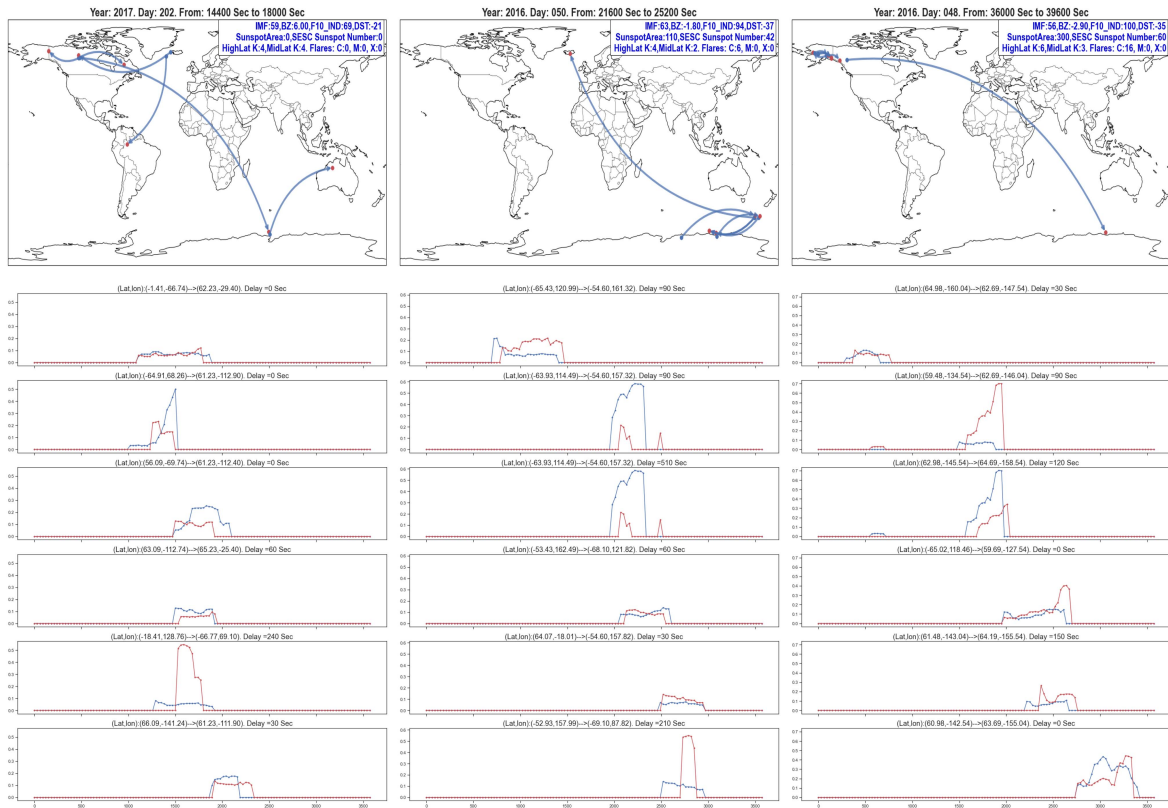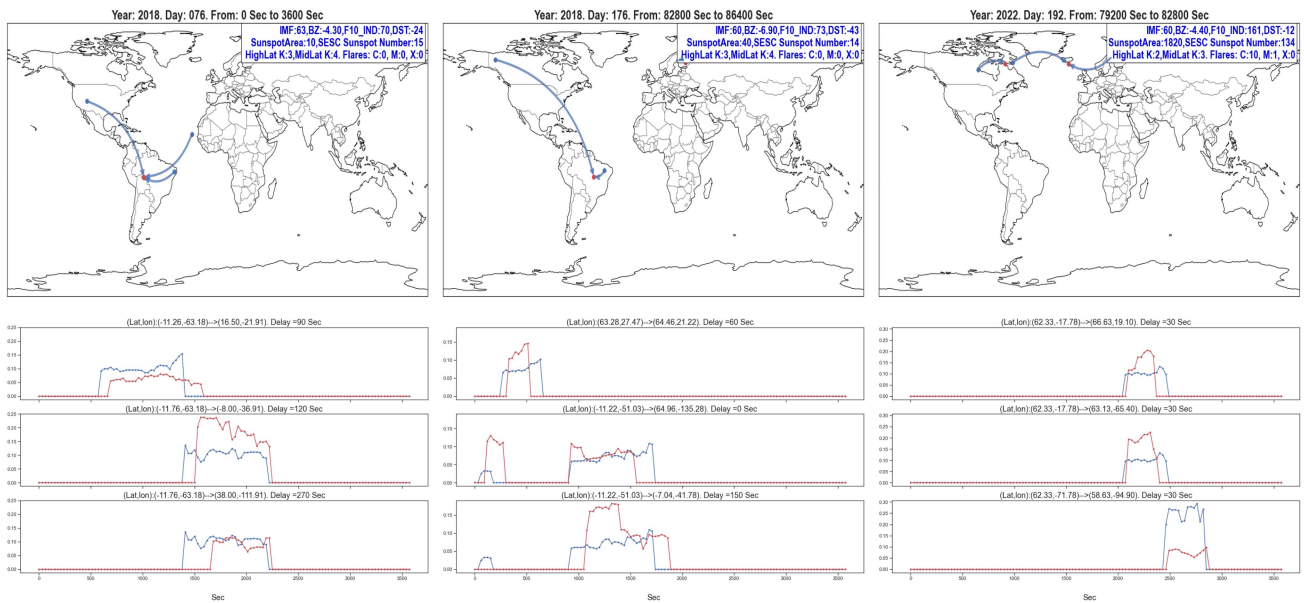

Fig. 16. Teleconnections and ROTI time series for a threshold of the $Bz < -3.3$ nT, (below percentile 10). ROTI range: 0.05–0.3 TECUs/min.

Fig. 17. Teleconnections and ROTI time series for a threshold of the $Bz > 2.6$ nT, (greater percentile 90). ROTI range: 0.05–0.45 TECUs/min.

Fig. 18. Teleconnections and ROTI time series for a threshold of the number of flares greater than 10. ROTI range: 0.05–0.5 TECUs/min.

TABLE II
TELECONNECTIONS DATES FOR ROTI THRESHOLD GREATER THAN 0.7 TECUS/MIN AND TOP GEOMAGNETIC STORMS [48]

Year	Teleconnection Dates	Geomagnetic storm
2016	January 13th, October 17th, and 22nd	No
2017	April 10th	No
2021	December 14th	No
2022	March 27th, and April 6th	No

Top Storms	1	2	3	4	5	6	7	8	9	10	11	12	13	14	15	16	17	18	19	20
2016 (day/month)	8/5	25/10	13/10	6/3	9/5	14/6	2/9	1/1	21/12	26/10	28/9	3/9	27/9	17/2	21/1	2/5	14/10	7/4	16/2	29/9
Kp	6+	6+	6+	6+	6+	6+	6	6	6	6-	6-	6-	6-	6-	6-	6-	6-	6-	5+	5+
2017 (day/month)	8/9	7/9	28/5	28/9	27/3	8/11	27/9	7/11	16/7	22/4	13/10	1/3	15/9	20/4	17/7	27/5	23/4	2/3	31/8	16/9
Kp	8+	8-	7	7-	6+	6+	6+	6+	6	6-	6-	6-	6-	6-	6-	6-	5+	5+	5+	5+
2021 (day/month)	4/11	12/5	12/10	3/11	20/3	1/3	20/5	17/9	30/11	14/3	2/3	16/4	25/4	15/6	25/3	19/12	28/8	17/4	21/3	3/3
Kp	8-	7	6+	6+	6-	6-	5+	5+	5+	5	5	5	5	5	5	5	5	5-	5-	5-
2022 (day/month)	17/8	10/4	4/9	13/3	14/4	3/10	26/12	7/8	14/1	14/3	4/2	5/3	3/2	30/11	22/10	19/1	28/11	27/9	21/7	7/7
Kp	7-	7-	6+	6+	6	6-	6-	6-	6-	6-	5+	5+	5+	5+	5+	5+	5+	5+	5+	5+

TABLE III
SPACE WEATHER DESCRIPTIVE STATISTICS BY FILTERING THRESHOLD

Case ROTI >0.5	mean	min	25%	50%	75%	max
BZ	-1.1	-17.9	-2.9	-0.9	0.8	8.1
DST	-16.9	-96	-28	-13	-3	27
FlaresX-RayC	2	0	0	0	2	17
FlaresX-RayM	0.2	0	0	0	0	5
FlaresX-RayX	0	0	0	0	0	1
PlanetaryKInd	2.9	0	2	3	4	7
HigLatKInd	2.8	0	1	3	4	9
MidLatKInd	2.4	0	1	2	3	6
RadioFlux10.7cm	93.1	66	75	84	108.5	166
SESCSunspotNum	41.5	0	13	31	64.5	147
SunspotArea	297.2	0	25	180	450	1760

Case ROTI >0.75	mean	min	25%	50%	75%	max
BZ	-0.7	-6.8	-2.5	-1.1	1.4	5.3
DST	-16.3	-44	-32	-17	2	19
FlaresX-RayC	0.6	0	0	0	1	4
FlaresX-RayM	0	0	0	0	0	0
FlaresX-RayX	0	0	0	0	0	0
PlanetaryKInd	3.2	0	2	3	5	6
HigLatKInd	3.5	0	2	4	5	8
MidLatKInd	2.9	0	2	3	4	6
RadioFlux10.7cm	84.2	73	75	81	84	130
SESCSunspotNum	27.3	0	11	26	40	97
SunspotArea	167.6	0	10	140	240	780

Case ROTI >1	mean	min	25%	50%	75%	max
BZ	-1.7	-6.8	-3.7	-2.4	-0.1	3.2
DST	-19.2	-44	-31.8	-22	-1.8	10
FlaresX-RayC	0.4	0	0	0	0	4
FlaresX-RayM	0	0	0	0	0	0
FlaresX-RayX	0	0	0	0	0	0
PlanetaryKInd	3.9	1	2.2	4	5	6
HigLatKInd	4.1	0	3	4	4.8	8
MidLatKInd	3.5	1	2.2	3.5	4	6
RadioFlux10.7cm	80.1	73	75	82	83.8	89
SESCSunspotNum	24.4	0	11	27.5	37.2	43
SunspotArea	137.1	0	10	140	240	260

Case ROTI >1.5	mean	min	25%	50%	75%	max
BZ	-2.5	-6.8	-4	-2.7	-2	2.6
DST	-25.2	-44	-37	-28	-17	2
FlaresX-RayC	0.2	0	0	0	0	1
FlaresX-RayM	0	0	0	0	0	0
FlaresX-RayX	0	0	0	0	0	0
PlanetaryKInd	4.2	2	3	4	6	6
HigLatKInd	4.8	3	3	4	6	8
MidLatKInd	3.7	2	3	4	4	6
RadioFlux10.7cm	80.1	73	75	83	83	84
SESCSunspotNum	24.9	0	11	29	43	43
SunspotArea	156.7	0	10	240	260	260

Case ROTI >2.0	mean	min	25%	50%	75%	max
BZ	-2.2	-6.8	-3.7	-2.6	-0.5	2.6
DST	-31.2	-44	-36	-30.5	-28	-17
FlaresX-RayC	0	0	0	0	0	0
FlaresX-RayM	0	0	0	0	0	0
FlaresX-RayX	0	0	0	0	0	0
PlanetaryKInd	4.7	3	4	4.5	5.8	6
HigLatKInd	4.8	3	4	4	5.5	8
MidLatKInd	4.2	3	3.2	4	4.8	6
RadioFlux10.7cm	81.3	73	81.5	83	83.8	84
SESCSunspotNum	30.2	11	26.8	29	39.5	43
SunspotArea	191.7	10	165	240	255	260

Case ROTI >2.5	mean	min	25%	50%	75%	max
BZ	-3.5	-6.8	-5.4	-4	-1.9	0.2
DST	-35	-44	-38.5	-33	-30.5	-28
FlaresX-RayC	0	0	0	0	0	0
FlaresX-RayM	0	0	0	0	0	0
FlaresX-RayX	0	0	0	0	0	0
PlanetaryKInd	5.3	4	5	6	6	6
HigLatKInd	5.7	3	4.5	6	7	8
MidLatKInd	4	3	3.5	4	4.5	5
RadioFlux10.7cm	82.7	81	82	83	83.5	84
SESCSunspotNum	32.7	26	27.5	29	36	43
SunspotArea	213.3	140	190	240	250	260

TABLE IV
DEFINITION OF THE SPACE WEATHER VARIABLES

Item	Description
Radio Flux	The Radio Flux at 10.7cm is a measure of the amount of radio energy emitted by the sun at such a wavelength. High solar flux values indicate an increased level of solar activity, typical during a few years around the solar cycle maximum epoch, repeated every 11 years approximately. When the high solar flux values are achieved very rapidly (at time scales of a few minutes), they use to be associated with solar flares. The radio flux measurement at 10.7 cm is typically expressed in units of solar flux units (SFU = 10^{-22} $W/m^2/Hz$).
SESC	The SESC (Solar-Equivalent Sunspot Count) Sunspot Number is a composite index that combines the number and total area of sunspots, account for the visibility, and the relative amount of magnetic flux in each sunspot. It is independently determined each day and it is based on the relative number of sunspots on the solar surface and is expressed as a number between 0 and 400. This number is a relative measure of the level of activity on the Sun.
Sunspot Area	Sunspot area refers to the size of a sunspot, or a group of sunspots on the surface of the Sun. Sunspots are areas of intense magnetic activity on the Sun's surface, that appear as dark spots due to their relatively low temperature. It is an important variable in space weather, closely related to the level of solar activity.
Solar Flares	Solar flares are intense and sudden bursts of energy that are emitted from sun spots groups on the Sun's surface, often accompanied by the ejection of plasma and charged particles into space. The categories by intensity are, from weakest to strongest: a) C-class flares: 10^{-7} to 10^{-6} (W/m^2) b) M-class flares: 10^{-5} to 10^{-4} (W/m^2) c) X-class flares: $\geq 10^{-4}$ (W/m^2)
IMF	The Interplanetary magnetic field (IMF) parameter, or IMF-PTS, (see [49]) is a measure of the strength and direction of the IMF, which is the solar magnetic field extended between planets in our solar system. The IMF-PTS parameter is a vector composed of three components defined versus the Sun-Earth plane (ecliptic): the horizontal components (Bx and By), and the vertical component (Bz). The IMF-PTS parameter can be used to study the structure and evolution of the IMF and its effects on the solar wind and the magnetosphere.
BZ-GSM	The Bz component of the IMF is the vertical component of the magnetic field versus the ecliptic and can influence the ionosphere by driving currents that in turn generate electric fields. When Bz is directed southward (negative), (See Figure 16) it can cause magnetic reconnection, a process where interplanetary magnetic field lines are reconnected with geomagnetic lines. This facilitates a direct entry and precipitation of the CME, and solar wind in general, charged particles towards high latitude regions of the Earth, with the corresponding release of energy [47]. This can lead to an increase in ionization and heating of the ionosphere, which can affect satellite-based communication and navigation systems.
SIGMA-Bz	The variance of the Bz component provides a measure of the spread or variability of the Bz values over a period of time. A high variance indicates that the Bz component is fluctuating rapidly, which can make it more difficult to predict the effects of the IMF on the Earth's magnetosphere and ionosphere.
DST	The Disturbance Storm Time (DST) index, in the case being significantly negative, measures the globally-averaged strength of a geomagnetic storm: It measures the deviation of the horizontal component of the equatorial magnetic field from its expected value during quiet times. The range of values for the DST Index is typically between -400 and +100 nT (nano Teslas): -100 nT or lower indicates a moderate to strong geomagnetic storm, while values below -250 nT indicate a severe geomagnetic storm. Positive values of the DST Index can occur during recovery periods following a geomagnetic storm.
KP	The KP index (or planetary index) is a measure of geomagnetic activity at high latitudes that ranges from 0 (quite geomagnetic conditions) to 9 (extreme geomagnetic activity) and characterizes the degree of disturbance of the Earth's magnetic field, obtained mostly from magnetometer readings at several high-latitude observatories around the world. The measurements of the KP indices that we have used in this study were; (1) High Latitude A KP: *HigLatAKInd*, (2) Mid Latitude A KP: *MidLatAKInd* and (3) Planetary A KP: *EstPlanetaryAKInd*.

Source of the space meather data [41], [40], [49], and [46].

REFERENCES

[1] I. V. Zhivetiev and Y. V. Yasyukevich, "Network theory to reveal ionospheric anomalies over North America and Australia," *Atmosphere*, vol. 13, no. 8, 2022, Art. no. 1333.

[2] N. Boers et al., "Complex networks reveal global pattern of extreme-rainfall teleconnections," *Nature*, vol. 566, no. 7744, pp. 373–377, 2019.

[3] E. Monte-Moreno, M. Hernandez-Pajares, and H. Yang, "Power law distribution of rapid ionosphere electron content fluctuations via GNSS measurements," *IEEE Trans. Geosci. Remote Sens.*, vol. 61, 2023, Art. no. 4105512.

[4] S. Mondal, A. K. Mishra, R. Leung, and B. Cook, "Global droughts connected by linkages between drought hubs," *Nature Commun.*, vol. 14, no. 1, 2023, Art. no. 144.

[5] A. Bhattacharyya, "Equatorial plasma bubbles: A review," *Atmosphere*, vol. 13, no. 10, 2022, Art. no. 1637.

[6] M. Piersanti et al., "On the magnetosphere-ionosphere coupling during the May 2021 geomagnetic storm," *Space Weather*, vol. 20, no. 6, 2022, Art. no. e2021SW003016.

[7] G. Li et al., "Low latitude ionospheric TEC oscillations associated with periodic changes in IMF bz polarity," *Geophysical Res. Lett.*, vol. 46, no. 16, pp. 9379–9387, 2019.

[8] L. P. Goncharenko et al., "Observations of pole-to-pole, stratosphere-to-ionosphere connection," *Front. Astron. Space Sci.*, vol. 8, 2022, Art. no. 768629.

[9] J. Y. Liu and S. A. Wu, "Global observations of ROTI by using ground-based GNSS receivers," *Terr., Atmospheric Ocean. Sci.*, vol. 32, pp. 519–530, 2021.

[10] J. Y. Liu and F. T. Berkey, "Phase relationships between total electron content variations, Doppler velocity oscillations, and geomagnetic pulsations," *J. Geophysical Res.: Space Phys.*, vol. 99, no. A9, pp. 17539–17545, 1994.

[11] J. T. Lin et al., "Rapid conjugate appearance of the giant ionospheric lamb wave signatures in the northern hemisphere after Hunga Tonga volcano eruptions," *Geophysical Res. Lett.*, vol. 49, no. 8, pp. 1–10, 2022.

[12] M.-Y. Chou, J. Yue, C. C. Lin, P. K. Rajesh, and N. M. Pedatella, "Conjugate effect of the 2011 Tohoku reflected tsunami-driven gravity waves in the ionosphere," *Geophysical Res. Lett.*, vol. 49, no. 3, 2022, Art. no. e2021GL097170.

[13] S.-R. Zhang et al., "Conjugate ionospheric perturbation during the 2017 solar eclipse," *J. Geophysical Res.: Space Phys.*, vol. 126, no. 2, 2021, Art. no. e2020JA028531.

[14] C. S. Carrano, C. E. Valladares, and K. M. Groves, "Latitudinal and local time variation of ionospheric turbulence parameters during the conjugate point equatorial experiment in Brazil," *Int. J. Geophys.*, vol. 2012, no. 1, 2012, Art. no. 103963.

[15] M. Schroeder, *Fractals, Chaos, Power Laws: Minutes From an Infinite Paradise*. North Chelmsford, MA, USA: Courier Corporation, 2009.

[16] J. Feder, *Fractals*. Berlin, Germany: Springer, 2013.

[17] J.-P. Chiles and P. Delfiner, *Geostatistics: Modeling Spatial Uncertainty*. Hoboken, NJ, USA: John Wiley and Sons, 2012.

[18] B. B. Mandelbrot, *Fractals and Scaling in Finance: Discontinuity, Concentration, Risk. Selecta Volume E*. Berlin, Germany: Springer Science and Business Media, 2013.

[19] M. Glymour, J. Pearl, and N. P. Jewell, *Causal Inference in Statistics: A Primer*. New York, NY, USA: Wiley, 2016.

[20] P. W. Holland, "Statistics and causal inference," *J. Amer. Stat. Assoc.*, vol. 81, no. 396, pp. 945–960, 1986.

[21] S. Basu, S. Basu, J. P. Aarons McClure, and M. D. Cousins, "On the coexistence of kilometer- and meter-scale irregularities in the nighttime equatorial F region," *J. Geophysical Res.*, vol. 83, pp. 4219–4226, 1978.

[22] Q. Quiroga, T. Kreuz, and P. Grassberger, "Event synchronization: A simple and fast method to measure synchronicity and time delay patterns," *Phys. Rev. E*, vol. 66, no. 4, 2002, Art. no. 041904.

[23] J. Fan et al., "Statistical physics approaches to the complex Earth system," *Phys. Rep.*, vol. 896, pp. 1–84, 2021.

[24] N. Boers et al., "Prediction of extreme floods in the eastern central andes based on a complex networks approach," *Nature Commun.*, vol. 5, no. 1, 2014, Art. no. 5199.

[25] N. Boers et al., "Complex networks identify spatial patterns of extreme rainfall events of the south American monsoon system," *Geophysical Res. Lett.*, vol. 40, no. 16, pp. 4386–4392, 2013.

[26] X. Pi, A. J. Mannucci, U. J. Lindqwister, and C. M. Ho, "Monitoring of global ionospheric irregularities using the worldwide GPS network," *Geophysical Res. Lett.*, vol. 24, no. 18, pp. 2283–2286, 1997.

[27] M. Hernández-Pajares et al., "The ionosphere: Effects, GPS modeling and the benefits for space geodetic techniques," *J. Geodesy*, vol. 85, no. 12, pp. 887–907, 2011.

[28] H. Lyu, M. Hernández-Pajares, M. Nohutcu, A. García-Rigo, H. Zhang, and J. Liu, "The Barcelona ionospheric mapping function (BIMF) and its application to northern mid-latitudes," *GPS Solutions*, vol. 22, 2018, Art. no. 67.

[29] C. Li, C. M. Hancock, N. A. Hamm, S. V. Veettil, and C. You, "Analysis of the relationship between scintillation parameters, multipath and ROTI," *Sensors*, vol. 20, no. 10, 2020, Art. no. 2877.

[30] R. K. Vankadara et al., "Signatures of equatorial plasma bubbles and ionospheric scintillations from magnetometer and GNSS observations in the Indian longitudes during the space weather events of early september 2017," *Remote Sens.*, vol. 14, no. 3, 2022, Art. no. 652.

[31] A. Ogwala et al., "Characterization of ionospheric irregularities over the equatorial and low latitude Nigeria region," *Astrophys. Space Sci.*, vol. 367, no. 8, 2022, Art. no. 79.

[32] C. S. Carrano, K. M. Groves, and C. L. Rino, "On the relationship between the rate of change of total electron content index (ROTI), irregularity strength (CkL), and the scintillation index (S4)," *J. Geophysical Res.: Space Phys.*, vol. 124, no. 3, pp. 2099–2112, 2019.

[33] S. Basu, K. M. Groves, J. M. Quinn, and P. Doherty, "A comparison of TEC fluctuations and scintillations at ascension island," *J. Atmospheric Sol.-Terr. Phys.*, vol. 61, no. 16, pp. 1219–1226, 1999.

[34] UPC, IonSAT - Ionospheric determination and navigation based on satellite and terrestrial systems, 2023. [Online]. Available: https://futur.upc.edu/IonSAT/p/3

[35] M. Hernández-Pajares, A. García-Rigo, J. M. Juan, J. Sanz, E. Monte, and A. Aragón-Àngel, "GNSS measurement of EUV photons flux rate during strong and mid solar flares," *Space Weather*, vol. 10, no. 12, 2012, Art. no. S12001.

[36] M. Caissy, L. Agrotis, G. Weber, M. Hernandez-Pajares, and U. Hugentobler, "Coming soon: The international GNSS real-time service, 2012," *Inside GNSS*, 2013.

[37] H. Yang, E. Monte-Moreno, M. Hernández-Pajares, and D. Roma-Dollase, "Real-time interpolation of global ionospheric maps by means of sparse representation," *J. Geodesy*, vol. 95, no. 6, 2021, Art. no. 71.

[38] P. Good, *Permutation Tests: A Practical Guide to Resampling Methods for Testing Hypotheses*. New York, NY, USA: Springer, 2013.

[39] Y. I. Beniguel et al., "MONITOR Iono Spheric Network: Two case studies on scintillation and electron content variability," *Annales Geophysicae*, vol. 35, no. 3, 2017, Art. no. 377.

[40] "National Oceanic and Atmospheric Administration (NOAA), Space weather prediction center (SWPC) of the national oceanic and atmospheric administration (NOAA)," 2023. [Online]. Available: https://www.swpc.noaa.gov/

[41] "National aeronautics and space administration, national aeronautics and space administration (NASA) website on solar physics and the sun's activity," 2023. [Online]. Available: https://www.nasa.gov/mission_pages/sunearth/spaceweather/index.html

[42] NOAA, Washington, DC, USA, "Space weather prediction center national oceanic and atmospheric administration. planetary K-index," 2023. [Online]. Available: https://www.swpc.noaa.gov/products/planetary-k-index

[43] NOAA, Washington, DC, USA, "Space weather prediction center national oceanic and atmospheric administration. 10.7 cm activity levels," 2023. [Online]. Available: https://www.swpc.noaa.gov/products/27-day-outlook-107-cm-radio-flux-and-geomagnetic-indices

[44] "Space weather data," 2023. [Online]. Available: https://www.spaceweatherlive.com/en/

[45] E. Monte-Moreno et al., "Method for forecasting ionospheric electron content fluctuations based on the optical flow algorithm," *IEEE Trans. Geosci. Remote Sens.*, vol. 60, 2022, Art. no. 5801821.

[46] NASA, Washington, DC, USA, "Heliophysics Datasets," 2023. [Online]. Available: https://cdaweb.gsfc.nasa.gov/misc/NotesO.html

[47] M. Kelly, *The Earth's Ionosphere: Plasma Physics and Electrodynamics*. New York, NY, USA: Elsevier, 2012.

[48] "Top 50 geomagnetic storms," 2023. [Online]. Available: https://www.spaceweatherlive.com/en/auroral-activity/top-50-geomagnetic-storms/

[49] NASA, Washington, DC, USA, "Definition of IMF-PTS," 2023. [Online]. Available: https://hpde.io/NASA/NumericalData-/OMNI/HighResolutionObservations/Version2/PT1M

Enric Monte-Moreno received the degree in telecomunication engineering from the Universitat Politecnica de Catalunya, Barcelona, Spain, in 1987, the Ph.D. degree in digital signal processing in 1992, the degree in philosophy and mathematics from Universidad Nacional a Distancia, in 2000, and the degree in mathematics in 2010.

He is currently an Associate Professor with the Department of Signal Theory and Communications, Universitat Politcnica de Catalunya. His research interests include digital signal processing, automatic speech recognition, GNSS, machine learning applied to economics, medical topics, and the study of the ionosphere.

Heng Yang received the Ph.D. degree in signal theory and processing from the Universitat Politècnica de Catalunya (UPC), Barcelona, Spain, in 2019.

He was a Postdoctoral Researcher with the Research Group of Ionospheric Determination and Navigation based on Satellite and Terrestrial Systems, Department of Mathematics, UPC. He is currently an Associate Professor at the School of Electronic Information and Engineering, Yangtze Normal University, Chongqing, China. He is working on the technologies of global navigation satellite system ionospheric sounding, including the computation of real-time global ionospheric maps, the detection of ionospheric perturbations, and the relationship with natural events.

Manuel Hernandez-Pajares received his educational degrees from the Universitat de Barcelona. He was the Chair of the International GNSS Service Ionosphere WG from 2002 to 2007, and a PI of tens of international scientific projects. Since 1989, he has been working on Global Navigation Satellite Systems and on new algorithms for precise ionospheric sounding and navigation, since 1994. He is currently a Full Professor and Head of the research group UPC-IonSAT, "Universitat Politècnica de Catalunya," Barcelona, Spain. He has authored or coauthored more than 100 papers in peer-reviewed journals within the first and second quartile of impact factor, with more than 5300 citations (h=35 and i10=93). He has also coauthored six patents, most of them international.